Journal of Computational Physics 404 (2020) 109132

Contents lists available at ScienceDirect

Journal of Computational Physics

www.elsevier.com/locate/jcp

On mass conservation and solvability of the discretized variable-density zero-Mach Navier-Stokes equations

Xiaoyi Lu [a,*], Carlos Pantano [a,b]

[a] Department of Mechanical Science and Engineering, University of Illinois at Urbana-Champaign, Urbana, IL 61801, USA
[b] Department of Aerospace and Mechanical Engineering, University of Southern California, Los Angeles, CA 90089, USA

ARTICLE INFO

Article history:
Received 4 April 2019
Received in revised form 20 October 2019
Accepted 13 November 2019
Available online 20 November 2019

Keywords:
Variable-density
Low-Mach number
DNS
Turbulent reacting flows
High-order methods

ABSTRACT

This paper presents a study of a variable-density zero-Mach Navier-Stokes discretization and subtle difficulties associated with the pressure. A consistent compatibility condition between the temperature and velocity is first derived. It is shown that one can accurately and efficiently solve all primitive variables with the uniform order of accuracy of the specified discretization and time-marching schemes. It is shown that higher density ratios than those commonly reported are achievable, and it is, in part, traced to the solvability of the pressure Poisson equation. Numerical properties are assessed with the method of manufactured solutions, and several classical testing cases are carried out to validate the code, ranging from variable-density mixing problems to premixed flames with forcing.

1. Introduction

Many numerical methods have been developed for incompressible and fully compressible flows [1–5]. In this respect, the zero-Mach formulation has been developed to study variable-density flows, where fluid motion is relatively slow compared to the speed of sound and density does not remain constant throughout owing to mixing, reacting, or other mechanisms [6]. Many variable-density subsonic flows, e.g., stratified flows and reacting flows, fall into this category. Using the fully compressible formulation to simulate these flows is very costly due to the stiffness introduced by the need to resolve small-scale acoustic waves that play little role in the dynamics. Therefore, it is more suitable to employ the variable-density Navier-Stokes equations in the zero-Mach number approximation, where the variable-density feature is retained, but acoustic waves are filtered out [6].

In general, there are two types of zero-Mach number approximations. The simplest form assumes the density is constant along pathlines ($\frac{D\rho}{Dt} = 0$), and the velocity field is solenoidal, i.e., divergence-free ($\nabla \cdot \boldsymbol{u} = 0$). Many numerical methods for this situation have been developed, see [7,8,4,9–14], where the divergence-free condition is a constraint enforcing mass conservation. The other form filters out the acoustic waves by decomposing pressure into two parts: dynamic and thermodynamic. The thermodynamic pressure is assumed to be constant in space. The dynamic pressure appears in the momentum equation but not in the temperature equation. The ratio of these two is the Mach number squared, thus small in these flows. The dilatation effect is preserved, and it is related to the thermal diffusion and scalar source terms but independent of thermodynamic pressure, [15–25], and it is the focus of this paper.

* Corresponding author.
E-mail address: xlu19@illinois.edu (X. Lu).

https://doi.org/10.1016/j.jcp.2019.109132
0021-9991/

It can be shown that at the heart of all zero-Mach flows is a saddle-point problem [26], which implies an elliptic equation for the pressure. Applying Schur complement reduction results in a constant-coefficient Poisson equation in solenoidal flows and a variable-coefficient Poisson equation in variable-density flows, even without introducing discretization, i.e., in the continuum sense. Solving this equation can have difficulties that may arise depending on the pressure boundary conditions being used [27]. The situation is so generic that one needs to consider a typical spatial/temporal method to realize some of the difficulties associated with solving the pressure problem. The choice of finite-difference/finite-volume spatial discretization is not crucial, although the problem does not appear in pseudo-spectral methods. To avoid artificial complications, we follow the standard procedure in the theory of differential-algebraic equations (DAEs) to derive a consistent *mass constraint* equation and pressure-Poisson equations for variable-density Navier-Stokes. This mass constraint equation is a compatibility condition between the continuity equation and a state relationship; both can be used to determine the density.

The concern about the solvability of the pressure is started by the observed difficulties reported by many colleagues in simulating variable-density flows at the zero-Mach limit with a maximum density variation of 6 to 8. Variable-density zero-Mach flows like premixed combustion [28–31,20,18,32,17], and buoyancy-driven flows, for example, Rayleigh-Taylor [24,23], Rayleigh-Bénard [33], and channel flow with heated walls [15] are typically simulated at this level of density variations. These simulations are often carried out in staggered grids when central finite-difference or finite-volume methods are employed. This is in part because this grid arrangement suppresses the spurious pressure mode caused by the well-known odd-even decoupling problem. However, the staggered method requires interpolations because the velocity components and pressure reside at different locations. Inevitably, this leads to more computational effort (in both implementation and calculations) and complicate mathematical formulations when the flow needs to be coupled with other computational modules, for example, boundary conditions or transport of other physical fields. The collocation method is superior in these aspects owing to its simple discretized form. However, the collocation method must ensure the pressure solvability condition without sacrificing the numerical accuracy. Previous literature proposed pressure-weighted interpolation [34] or special flux-splitting method [35]. As discussed in [36], these propositions do not fulfill solvability unconditionally while retaining time accuracy. Rauwoens [36] used a compact stencil for the discretized Laplacian and a flux correction term to remove the spurious pressure mode. In this paper, we propose an approach to ensure the pressure solvability condition and also show that a uniform order of accuracy for all fields can be achieved even when the density ratio becomes large. The solution procedure also employed a compact discrete Laplacian for the pressure. Unlike [36], the time integration here advances the temperature field and then update the density via an algebraic relationship. In addition, the correction to the right-hand side of the pressure equation is determined by algebraic considerations. Lastly, we demonstrate the methodology in a few large-scale problems.

2. Governing and derived equations

Variable-density flows in the zero-Mach limit are governed by the conservation laws of mass, momentum, and energy. Here we consider the governing equations in non-conservation form in the domain Ω, given non-dimensionally by

$$\frac{\partial \rho}{\partial t} + \nabla \cdot (\rho \boldsymbol{u}) = 0, \tag{1}$$

$$\rho \left(\frac{\partial \boldsymbol{u}}{\partial t} + \boldsymbol{u} \cdot \nabla \boldsymbol{u} \right) = -\nabla p + \nabla \cdot \boldsymbol{\tau} + \rho \boldsymbol{f}, \tag{2}$$

$$\rho \left(\frac{\partial \phi_j}{\partial t} + \boldsymbol{u} \cdot \nabla \phi_j \right) = \frac{1}{Pe_j} \nabla^2 \phi_j + \varpi_j, \tag{3}$$

where the boundary and initial conditions are given in the generic form

$$(\boldsymbol{u}, \phi_j) = \boldsymbol{h}_0, \quad \boldsymbol{x} \in \Omega, \quad t = 0, \tag{4}$$

$$\mathcal{B}_D(\boldsymbol{u}, \phi_j) = \boldsymbol{g}_D, \quad \boldsymbol{x} \in \partial\Omega_D, \quad t \geq 0, \tag{5}$$

$$\mathcal{B}_N(\boldsymbol{u}, p, \phi_j) = \boldsymbol{g}_N, \quad \boldsymbol{x} \in \partial\Omega_N, \quad t \geq 0. \tag{6}$$

Density, velocity, pressure, and scalars are denoted by ρ, $\boldsymbol{u}$, p, ϕ_j, respectively, where $j = 0, \ldots, m$. A body force $\boldsymbol{f}(\boldsymbol{x}, t)$ and scalar source term $\varpi_j(\boldsymbol{x}, t, \phi_l)$ are included for generality. It is assumed that ϕ_0 denotes temperature and that p includes the isotropic viscous dilatation term (valid in the constant viscosity simplification). The viscous stress tensor $\boldsymbol{\tau} = \frac{1}{Re} \left(\nabla \boldsymbol{u} + \nabla \boldsymbol{u}^T - \frac{2}{3} \nabla \cdot \boldsymbol{u} \right)$ is assumed to be equivalent to $\nabla \cdot \boldsymbol{\tau} = \frac{1}{Re} \nabla^2 \boldsymbol{u}$; constant viscosity and corresponding reinterpretation of the pressure. The Reynolds and Peclet numbers, Re and Pe_j, are assumed constant, but temperature-dependent transport coefficients can also be considered by employing the appropriate expressions if needed. It is equally possible to use the conservation form of the equations, although some authors prefer the non-conservation form for variable density flows [37]. The numerical solution procedure of these equations discussed in this paper apply to both formulations (which are equivalent in the continuous form). The mathematical statement of the problem also requires suitable conditions at the boundary $\partial\Omega$, which is decomposed into Dirichlet and Neumann parts $\partial\Omega_D$ and $\partial\Omega_N$, respectively. The Dirichlet-type and

Neumann-type conditions are expressed in terms of boundary operators $\mathcal{B}_D$ and $\mathcal{B}_N$, respectively, along with the corresponding boundary data vectors $\boldsymbol{g}_D$ and $\boldsymbol{g}_N$. $\boldsymbol{h}_0$ denotes the initial fields for all variables inside the domain Ω.

For ideal gases in the zero-Mach number limit, density and temperature have a one-to-one mapping relation referred to as a *state relationship* (SR), which ignoring changes in mean molecular weight can be written in a non-dimensional form as

$$\rho(\phi_0) = \frac{1}{1-\alpha\phi_0}, \tag{7}$$

with the corresponding thermal expansion coefficient α (here considered constant). We have purposely ignored many subtle details of the governing equations such as temperature-dependent transport coefficients and variation of mean molecular weight with composition to avoid distraction from the fundamental difficulties of solving these equations. It is fully acknowledged that these details need to be included for accurate predictions, which will require straight-forward modifications to the subsequent discussion.

Now, the density can be obtained by either solving Eq. (1) or by using ϕ_0 in Eq. (7). Both approaches are equivalent only if an additional condition is satisfied. To extract this condition, we write the equations as follows

$$\rho\frac{\partial}{\partial t}\begin{bmatrix}\phi_j\\ \boldsymbol{u}\end{bmatrix} = \begin{bmatrix}\frac{1}{Pe_j}\nabla^2\phi_j - \rho\boldsymbol{u}\cdot\nabla\phi_j + \varpi_j\\ -\nabla p - \rho\boldsymbol{u}\cdot\nabla\boldsymbol{u} + \frac{1}{Re}\nabla^2\boldsymbol{u} + \rho\boldsymbol{f}\end{bmatrix} = \begin{bmatrix}-\mathcal{D}(\phi_j) + \varpi_j\\ -\nabla p - \boldsymbol{\mathcal{N}}(\boldsymbol{u}) + \rho\boldsymbol{f}\end{bmatrix}, \tag{8}$$

which introduces the operators $\mathcal{D}(\phi_j)$ and $\boldsymbol{\mathcal{N}}(\boldsymbol{u})$ for convenience, and we have omitted denoting that $\boldsymbol{\mathcal{N}}$ depends on $\rho\boldsymbol{u}$ for simplicity. These governing equations form a system of DAEs when Eq. (7) is included. The compatibility condition between temperature and velocity is obtained by lowering the differentiation index of the DAE system (a measure for the distance between DAEs to ODEs, see [38]). This is accomplished by successively taking time derivative of SR and substituting the governing equations of the primitive fields as needed. This process will lead to the *mass constraint* equation. First, take the time derivative of SR, which reads

$$\frac{\partial\rho}{\partial t} - \alpha\rho^2\frac{\partial\phi_0}{\partial t} = 0, \tag{9}$$

then substitute the partial derivatives of ρ and ϕ_0 with respect to time from Eq. (1) and Eq. (3), respectively, and simplify, resulting in

$$\mathcal{C}(\rho\boldsymbol{u},\phi_0) = \frac{1}{\rho}\nabla\cdot(\rho\boldsymbol{u}) + \alpha[\varpi_0 - \mathcal{D}(\phi_0)] = 0. \tag{10}$$

Note that the counterpart of the mass constraint, Eq. (10), in constant-density flows is the divergence-free condition, which can be obtained by setting $\alpha = 0$ above. In general, the expression of the mass constraint depends on the underlying SR. Without loss of generality, the numerical methods presented in the paper use Eq. (7) as an example. For other forms of SRs, the dependence of the density on temperature $\frac{\partial\rho}{\partial\phi_0}$ in Eq. (9) may be different, resulting in different terms that relate the dilatation of the flow and the convection and dissipation of the temperature field.

As it is well known, the pressure is responsible of enforcing mass conservation. The consistent pressure equation for variable-density flow is derived by further time-differentiating the mass constraint, Eq. (10), and substituting governing equations for the partial derivatives of $\boldsymbol{u}$ and ϕ_0 with respect to time, giving the pressure Poisson-like equation (PPE) for variable-density flows

$$-\nabla\cdot\left(\frac{1}{\rho}\nabla p\right) = \nabla\cdot\left[\frac{1}{\rho}\boldsymbol{\mathcal{N}}(\boldsymbol{u}) - \boldsymbol{f}\right] + \alpha\left[\frac{1}{Pe_0}\nabla^2 + \frac{\partial\varpi_0}{\partial\phi_0}\right]\frac{1}{\rho}\left[\mathcal{D}(\phi_0) - \varpi_0\right] - \alpha\frac{\partial\varpi_0}{\partial t}, \tag{11}$$

where the second term in the right-hand side employs the functional derivative of ϖ_0 with respect to ϕ_0 and the temporal derivative in the last term is assumed to contain contributions of the partial time derivatives of ϕ_j for $j = 1, \ldots, m$. Once again, the PPE for constant-density flows can be retrieved by simply setting $\alpha = 0$ above. Note also that we have not implied or used the chain rule of differentiation in spatial derivatives at any stage in order for these expressions to remain valid when the equations are semi-discretized. It is evident that explicitly calculating the right-hand side of Eq. (11) can be computationally intensive and cumbersome. This paper presents a numerical method for Eq. (8) and Eq. (10) which is obviously an index-1 DAE system.

Now, it is well known that the mass constraint, Eq. (10), is required to be held true initially, $t = 0$, in order to prevent the appearance of spurious temporal transients, see [39] and [40], that if not handled correctly may destroy the convergence of the solution under time and space refinement. Furthermore, directly using the variable-coefficient Laplacian operator in Eq. (11) to compute the pressure introduces high computational cost in large-scale simulations, see [11]. Therefore, for computational efficiency reasons, one would like to avoid solving Eq. (11) directly and instead apply an appropriate temporal numerical approximation that enforces Eq. (10). One typical numerical discretization that avoids high computational cost is discussed next. The choice below is dictated by its popularity in CFD solvers, but modifications to other time integrators of similar structure can also be carried out without difficulties. The large literature on DAE discusses other choices and convergence results for more general problems, see [38,39]. Here, we focus on specific difficulties of the variable-density (non-dilatation-free) Navier-Stokes problem.

3. A numerical method

The numerics of constant-density Navier-Stokes equations are well understood [41,2,3,1] but their corresponding variable-density details are more subtle [16,42]. Here, as a generic approach, we consider the popular semi-implicit second-order Adams-Bashforth/Crank-Nicolson (AB/CN) time marching method. Nevertheless, other time integration strategies are also possible with the corresponding modifications in the formulae below. At the same time, we will consider spatial central differentiation approximations of 2nd, 4th, and 6th order as well as a pseudo-spectral method for periodic problems. The focus is on the collocated discretization, implying an approximate projection method, because it can result in efficient solvers for large problems when correctly formulated. We will focus on some subtle difficulties that one encounters when solving the system of Eq. (8) and Eq. (10) numerically.

3.1. Semi-discretization

The governing differential equations are discretized in space using a pseudo-spectral approximation for periodic problems or by finite differences for non-periodic problems. In the latter case, the boundary conditions are enforced with a penalty-based approach known as the Summation-By-Parts/Simultaneous-Approximation-Terms (SBP/SAT) method, see [43,44] for the overview of this family of methods. The SBP/SAT method imposes boundary conditions in a weak sense by introducing penalty terms into the governing equations and using finite-differencing operators that preserve SBP properties [45,46] to ensure numerical stability of the boundary treatment.

The discrete gradient, ∇_h, and Laplacian, ∇_h^2, operators in two dimensions are defined by

$$\nabla_h = D_x \otimes I_y + I_x \otimes D_y, \quad \nabla_h^2 = D_x^2 \otimes I_y + I_x \otimes D_y^2, \quad I = I_x \otimes I_y, \tag{12}$$

respectively, where $\otimes$ denotes the Kronecker product. Similarly, this can be extended to three dimensions. The subscript h denotes the characteristic grid spacing which may be different in each direction. $I_x \in \mathbb{R}^{N_x \times N_x}$, $I_y \in \mathbb{R}^{N_y \times N_y}$ and $I \in \mathbb{R}^{N_x N_y \times N_x N_y}$ denote the identity matrices, where N_x and N_y are the collocation grid points along x and y direction, respectively. D and D^2 denote first- and second-order differentiation matrices, respectively, where subscripts x and y denote the corresponding coordinate directions. The matrix D^2 denotes the proper second-order derivative approximation and it should not be confused by the matrix product DD. The detailed differentiation matrices D and D^2 can be found in [46] for the finite-difference methods of different orders of accuracy. Note that the finite-differencing matrices have been extended to include SBP boundary stencils. Next, it is understood that ρ, $\boldsymbol{u}$ and ϕ_j denote the discrete grid functions corresponding to their continuous fields in the equations above. This cannot lead to confusion because the grid function and the continuous fields cannot appear in the same equations. The discretized equations can be readily and compactly written in terms of the following density-weighted operators:

$$K_\rho = \frac{1}{\rho Pe}\nabla_h^2, \quad \boldsymbol{V}_\rho = \frac{1}{\rho Re}\begin{bmatrix} \nabla_h^2 & 0 \\ 0 & \nabla_h^2 \end{bmatrix}, \quad \boldsymbol{G}_\rho = \frac{1}{\rho}\nabla_h, \tag{13}$$

where the density in the denominator denotes the value of the density at the grid location where each operator (on the right-hand side) returns its value, i.e., the finite-difference convention (one could also interpret it in terms of a diagonal matrix with the inverse of the density injected in the diagonal). The scalar operators for different j are not identical owing to the possibly different Peclet numbers of each species. However, we have omitted the subscript j as long as it does not cause confusions.

The nonlinear skew-symmetric operator used to discretize the advective part of the equations is given by

$$\boldsymbol{N}_\rho(\boldsymbol{u}, \square) = \frac{1}{2\rho}\left[\nabla_h \cdot (\rho \boldsymbol{u} \square) + \rho \boldsymbol{u} \cdot \nabla_h \square - \nabla_h \cdot (\rho \boldsymbol{u})\, \square\right], \tag{14}$$

where the symbol $\square$ stands as a placeholder for a given field, and the above form is preferred for better stability properties as compared to the direct discretization of the continuous operator; see [47] for the constant-density and [48] for the conservative form of the governing equations for variable density. Here, we use the non-conservative form of the skew-symmetric operator. The difference between the conservative skew-symmetric operator and the non-conservative above is the change in sign in the last term of Eq. (14) and division by ρ. Eq. (8) can now be expressed as

$$\frac{d}{dt}\begin{bmatrix} \phi_j \\ \boldsymbol{u} \end{bmatrix} = \begin{bmatrix} K_\rho \phi_j - N_\rho(\boldsymbol{u}, \phi_j) + \frac{1}{\rho}\varpi_j + S_\rho(\phi_j) \\ \boldsymbol{V}_\rho \boldsymbol{u} - \boldsymbol{N}_\rho(\boldsymbol{u}, \boldsymbol{u}) - \boldsymbol{G}_\rho p + \boldsymbol{f} + S_\rho(\boldsymbol{u}) \end{bmatrix}, \tag{15}$$

while the discrete mass constraint, Eq. (10), is given by

$$C(\rho \boldsymbol{u}, \phi_0) = \frac{1}{\rho}\nabla_h \cdot (\rho \boldsymbol{u}) + \alpha\left[\rho\left(K_\rho \phi_0 - N_\rho(\boldsymbol{u}, \phi_0) + S_\rho(\phi_0)\right) + \varpi_0\right] = 0. \tag{16}$$

The boundary information is incorporated in the SAT penalty terms which are given by

$$S_\rho(\phi_j) = S^a_\rho(\phi_j) + S^d_\rho(\phi_j), \quad S_\rho(\boldsymbol{u}) = S^a_\rho(\boldsymbol{u}) + S^d_\rho(\boldsymbol{u}) + S^g_\rho(\boldsymbol{u}). \tag{17}$$

Note that finite-difference operators have been extended with a set of boundary stencils, see [46]. Therefore, for each term that involves spatial discretization, there is a corresponding SAT term [49]. Those introduced by advection, diffusion, and pressure gradient, are denoted with superscript a, d, and g, respectively. The definitions of these SAT terms, their derivation for Navier-Stokes equations, and other related aspects are explained in Appendix B. As for periodic problems, without boundary stencils, SAT terms simply vanish.

Now, we adopt the usual splitting of the equations where advection is treated explicitly using an Adams-Bashforth (AB) method while diffusion is treated implicitly using a Crank-Nicolson (CN) method. Pressure is assumed to be defined at the intermediate (staggered) time $n+1/2$. This time-discretization is second-order accurate and in principle has better stability performance than a purely explicit method of the same order; see [7] for the stability and order-of-accuracy analysis. Equation 15 discretized by the semi-implicit AB/CN with constant time step Δt, generalization to variable time-step size is straightforward, reads

$$\begin{aligned}\frac{\phi_j^{n+1}-\phi_j^n}{\Delta t} &= \frac{3}{2}\left[\frac{1}{\rho^n}\varpi_j^n - N_{\rho^n}(\boldsymbol{u}^n,\phi_j^n) + S^a_{\rho^n}(\phi_j^n)\right] - \frac{1}{2}\left[\frac{1}{\rho^{n-1}}\varpi_j^{n-1} - N_{\rho^{n-1}}(\boldsymbol{u}^{n-1},\phi_j^{n-1}) + S^a_{\rho^{n-1}}(\phi_j^{n-1})\right] \\ &\quad + \frac{1}{2}\left[K_{\rho^{n+1}}\phi_j^{n+1} + S^d_{\rho^{n+1}}(\phi_j^{n+1})\right] + \frac{1}{2}\left[K_{\rho^n}\phi_j^n + S^d_{\rho^n}(\phi_j^n)\right], \end{aligned}\tag{18}$$

$$\begin{aligned}\frac{\boldsymbol{u}^{n+1}-\boldsymbol{u}^n}{\Delta t} &= \frac{3}{2}\left[\boldsymbol{f}^n - \boldsymbol{N}_{\rho^n}(\boldsymbol{u}^n,\boldsymbol{u}^n) + S^a_{\rho^n}(\boldsymbol{u}^n)\right] - \frac{1}{2}\left[\boldsymbol{f}^{n-1} - \boldsymbol{N}_{\rho^{n-1}}(\boldsymbol{u}^{n-1},\boldsymbol{u}^{n-1}) + S^a_{\rho^{n-1}}(\boldsymbol{u}^{n-1})\right] \\ &\quad + \frac{1}{2}\left[\boldsymbol{V}_{\rho^{n+1}}\boldsymbol{u}^{n+1} + S^d_{\rho^{n+1}}(\boldsymbol{u}^{n+1})\right] + \frac{1}{2}\left[\boldsymbol{V}_{\rho^n}\boldsymbol{u}^n + S^d_{\rho^n}(\boldsymbol{u}^n)\right] - \boldsymbol{G}_{\rho^{n+1/2}}p^{n+1/2} + S^g_{\rho^{n+1/2}}(\boldsymbol{u}^{n+1/2}), \end{aligned}\tag{19}$$

where n denotes the time index and $t^{n+1}-t^n=\Delta t$. The density in the pressure term of Eq. (19) is defined by

$$\frac{1}{\rho^{n+1/2}} = \frac{1}{2}\left(\frac{1}{\rho^n}+\frac{1}{\rho^{n+1}}\right), \tag{20}$$

although the arithmetic mean is also possible. The equations are advanced in time subject to a CFL-like time-step restriction where

$$\mathrm{CFL} = \Delta t \sum \frac{|u_k|_{\max}}{\Delta x_k} < \text{constant} \sim 1, \tag{21}$$

independent of viscosity (owing to the semi-implicit treatment of diffusive terms). In order to focus on the main issue here, which is how to solve Eqs. (18)-(19), SAT penalty terms (for the non-periodic problems) are omitted in the following discussion, although they are incorporated in the examples later. We emphasize that the problem we address here is that although one can construct discrete equations by many different approaches, this does not mean that the equations have a solution. This is the focus of the paper.

Inspection of the equations shows that one can solve for scalars at the next time level first, before the velocity is updated; one of the desirable features of the AB/CN splitting. Algebraic manipulations of Eq. (18) give the following delta-form implicit system of equations

$$\left(\tilde{I}_j - \frac{\Delta t}{2}K_{\rho^{n+1}}\right)\delta\phi_j = \Delta t\left[\tilde{K}_\rho\phi_j^n + \frac{3}{2}\left(\frac{1}{\rho^n}\varpi_j^n - N_{\rho^n}(\boldsymbol{u}^n,\phi_j^n)\right) - \frac{1}{2}\left(\frac{1}{\rho^{n-1}}\varpi_j^{n-1} - N_{\rho^{n-1}}(\boldsymbol{u}^{n-1},\phi_j^{n-1})\right)\right], \tag{22}$$

where $\delta\phi_j = \phi_j^{n+1}-\phi_j^n$ and

$$\tilde{I}_0 = I + \alpha\frac{\Delta t}{2}[\rho^n][K_{\rho^n}\phi_0^n] \qquad \tilde{K}_\rho = K_{\rho^n} \qquad j=0, \tag{23}$$

$$\tilde{I}_j = I \qquad \tilde{K}_\rho = \frac{1}{2}\left(K_{\rho^n} + K_{\rho^{n+1}}\right) \qquad j>0. \tag{24}$$

Note that we have used the relation $\frac{1}{\rho^{n+1}} - \frac{1}{\rho^n} = -\alpha\delta\phi_0$ to define $\tilde{I}_0$ and denote by $[\psi]$ the diagonal matrix constructed from the vector ψ (being arbitrary). The equation for the temperature is nonlinear in general because it involves $K_{\rho^{n+1}}$ and requires iteration. In all our examples, we simply use a Picard iteration to solve for $\delta\phi_0$ and update the density at the next time level, ρ^{n+1}, using $\phi_0^{n+1}=\phi_0^n+\delta\phi_0$ and Eq. (7). After convergence of this iteration, the remaining scalar equations are linear and can be solved at once. Note that a Strang splitting technique is better suited when the source term is stiff [50,32,29]; something not considered here.

Let $\delta\boldsymbol{u} = \boldsymbol{u}^{n+1}-\boldsymbol{u}^n$ and $\hat{p}=\Delta t p^{n+1/2}$, and define the operators

$$\boldsymbol{A}_\rho = \boldsymbol{I} - \frac{\Delta t}{2}\boldsymbol{V}_\rho, \quad \tilde{\boldsymbol{V}}_\rho = \frac{1}{2}\left(\boldsymbol{V}_{\rho^n} + \boldsymbol{V}_{\rho^{n+1}}\right), \quad Q_{\rho^{n+1}}\square = [\rho^{n+1}]^{-1}\nabla_h\cdot(\rho^{n+1}\square) - \alpha[\rho^{n+1}]N_{\rho^{n+1}}(\square,\phi_0^{n+1}), \tag{25}$$

allowing Eq. (19) to be written as

$$\boldsymbol{A}_{\rho^{n+1}}\delta\boldsymbol{u}+\boldsymbol{G}_{\rho^{n+1/2}}\hat{p}=\boldsymbol{a} \equiv \Delta t\left[\tilde{\boldsymbol{V}}_{\rho}\boldsymbol{u}^{n}+\frac{3}{2}\left[\boldsymbol{f}^{n}-\boldsymbol{N}_{\rho^{n}}(\boldsymbol{u}^{n},\boldsymbol{u}^{n})\right]-\frac{1}{2}\left[\boldsymbol{f}^{n-1}-\boldsymbol{N}_{\rho^{n-1}}(\boldsymbol{u}^{n-1},\boldsymbol{u}^{n-1})\right]\right], \tag{26}$$

with the mass-conservation constraint, Eq. (16), enforced at the end of the step, by

$$Q_{\rho^{n+1}}\delta\boldsymbol{u}=-C(\rho^{n+1}\boldsymbol{u}^{n},\phi_{0}^{n+1}). \tag{27}$$

There are numerous strategies to solve the velocity-pressure coupled system, Eqs. (26)-(27), and we discuss the pressure projection approach next. Other formulations have been discussed by [51,4] but the problem we address below is generic and it will apply to other formulations as well.

3.2. Pressure projection

In this section we focus on a strategy that can be implemented efficiently to solve large-scale variable-density flow problems and avoid discussion of other methods that require the assembly or inversion of large matrices. An overview of pressure projection methods for constant-density incompressible Navier-Stokes equations can be found in [4]. The non-incremental projection method in [4] that we favor consists of two steps, which has been extended for variable-density flows. First, one solves for an intermediate velocity variable $\delta\boldsymbol{u}^{*}$ by ignoring the contribution of the pressure gradient, like in a fractional step method, according to

$$\boldsymbol{A}_{\rho^{n+1}}\delta\boldsymbol{u}^{*}=\boldsymbol{a}. \tag{28}$$

Second, the momentum equations are rearranged, subtracting Eq. (28) from Eq. (26) and using $\boldsymbol{u}^{*}=\boldsymbol{u}^{n}+\delta\boldsymbol{u}^{*}$, to give

$$\begin{bmatrix}\boldsymbol{A}_{\rho^{n+1}} & \boldsymbol{G}_{\rho^{n+1/2}}\\ Q_{\rho^{n+1}} & 0\end{bmatrix}\begin{bmatrix}\delta\boldsymbol{z}\\ \hat{p}\end{bmatrix}=\begin{bmatrix}0\\ -C(\rho^{n+1}\boldsymbol{u}^{*},\phi_{0}^{n+1})\end{bmatrix}, \tag{29}$$

where $\delta\boldsymbol{z}=\boldsymbol{u}^{n+1}-\boldsymbol{u}^{*}=\delta\boldsymbol{u}-\delta\boldsymbol{u}^{*}$. Equation 29 exposes explicitly the well-known saddle-point structure of the momentum-pressure coupling, highlighting here that in general $Q_{\rho^{n+1}}$ is not the transpose of $\boldsymbol{G}_{\rho^{n+1/2}}$ for variable-density flows. The corresponding system of equations for incompressible flows are given by

$$\begin{bmatrix}\boldsymbol{A} & \boldsymbol{G}\\ \boldsymbol{C} & 0\end{bmatrix}\begin{bmatrix}\delta\boldsymbol{z}\\ \hat{p}\end{bmatrix}=\begin{bmatrix}\boldsymbol{A} & \boldsymbol{G}\\ 0 & -\boldsymbol{C}\boldsymbol{A}^{-1}\boldsymbol{G}\end{bmatrix}\begin{bmatrix}\delta\boldsymbol{z}\\ \hat{p}\end{bmatrix}=\begin{bmatrix}0\\ -\boldsymbol{C}\boldsymbol{u}^{*}\end{bmatrix}, \tag{30}$$

where we have eliminated the subscript ρ since the density is constant. As previously mentioned, operators $\boldsymbol{Q}_{\rho}$ and $\boldsymbol{C}_{\rho}$ are both reduced to the divergence operator $\boldsymbol{C}$ and equal to the transpose of the gradient operator $\boldsymbol{G}$ in the constant-density case.

The systems of equations like Eq. (29) and Eq. (30) are saddle-point problems [26]. Simultaneous solution of the velocity and pressure typically requires a Krylov-space method, e.g. GMRES, of large size owing to the indefiniteness of the system and therefore it is not desirable. This type of methods is often accelerated with specially designed preconditioners. Here, the true Schur complement method [1] is also impractical because the inverse of $\boldsymbol{A}_{\rho^{n+1}}$ is dense and changes in time as shown in Eq. (30). Therefore, a good strategy is to form an approximate factorization [51] to express the system in a form that is amenable to block iteration. It is postponed to § 3.3 the subtle solvability issue of the linear systems, which depends on the boundary conditions.

Multiplying the first row of Eq. (29) by $Q_{\rho^{n+1}}R$, where $R=[\rho^{n+1}]^{-1}[\rho^{n+1/2}]$, and subtracting from the second row and using the definition of $\boldsymbol{A}_{\rho^{n+1}}$, Eq. (25), one can rewrite Eq. (29) as follows

$$\begin{bmatrix}\boldsymbol{A}_{\rho^{n+1}} & \boldsymbol{G}_{\rho^{n+1/2}}\\ Q_{\rho^{n+1}}\left(\boldsymbol{I}-R\boldsymbol{A}_{\rho^{n+1}}\right) & -Q_{\rho^{n+1}}R\boldsymbol{G}_{\rho^{n+1/2}}\end{bmatrix}\begin{bmatrix}\delta\boldsymbol{z}\\ \hat{p}\end{bmatrix}=\begin{bmatrix}0\\ -C(\rho^{n+1}\boldsymbol{u}^{*},\phi_{0}^{n+1})\end{bmatrix}. \tag{31}$$

Observe that this system would be approximately in Schur-complement form if the viscous term had been integrated explicitly in time because $\boldsymbol{A}_{\rho^{n+1}}$ would be the identity matrix and the lower off-diagonal block matrix would be approximately zero since $R=I+\mathcal{O}(\Delta t)$. The first equality of Eq. (30) shows the Schur complement form for the incompressible problem. If an explicit time integration is used, the Schur complement matrix is well-approximated by a Laplacian operator (recall that $\nabla_{h}^{2}\sim\nabla_{h}\cdot\nabla_{h}=\boldsymbol{C}\boldsymbol{G}$). Also note that the process to arrive at Eq. (31) is equivalent, in the constant-density case, to taking the discrete divergence of the momentum equation. Therefore, it is reasonable to expect that a solution based on Eq. (31) may work as well as the true Schur complement for the pressure. Now, Eq. (31) is in general ill-posed when using a collocated grid and this can be made clear by expanding the lower diagonal term, which results in

$$-Q_{\rho^{n+1}} R\boldsymbol{G}_{\rho^{n+1/2}} = -[\rho^{n+1}]^{-1}\nabla_h \cdot \nabla_h + \alpha\rho^{n+1}\boldsymbol{N}_{\rho^{n+1}}\left([\rho^{n+1}]^{-1}\nabla_h\Box, \phi_0^{n+1}\right). \tag{32}$$

Observe that Eq. (32) is still not in a satisfactory form because the operator $\nabla_h \cdot \nabla_h$ is too wide in a collocated mesh arrangement and it has a null space of dimension larger than one (beyond the hydrostatic kernel mode). This is quite evident in the constant-density case where $\alpha = 0$, but a problem that is still present in variable-density flow, $\alpha \neq 0$, and can result in an ill-posed system since the additional term $\boldsymbol{N}_{\rho^{n+1}}$ in Eq. (32) does not really remove the difficulty. One can circumvent the solvability issue by resorting to the staggered method, at a cost. It is often not a trivial task to couple the staggered flow solver with other computational components and extend to 3D coordinates. Although some previous researchers have achieved this [21], the staggered method still constantly requires interpolations while constructing nearly every nonlinear term. It is conceivable that a collocated method is computationally more efficient. As for the collocated method, the solution of the system Eq. (31) is obtainable only if one applies a residual minimization method and accepts the least-square solution.

It is at this point that the approximate projection method is introduced. The wide operator $\nabla_h \cdot \nabla_h$ is replaced with the narrow ∇_h^2 that does not suffer from an enlarged null space and we admit a discretization error of the size of the spatial approximation order. Therefore, we introduce the modified operator

$$-(Q_{\rho^{n+1}} R\boldsymbol{G}_{\rho^{n+1/2}})^* = -[\rho^{n+1}]^{-1}\nabla_h^2 + \alpha\rho^{n+1}\boldsymbol{N}_{\rho^{n+1}}\left([\rho^{n+1}]^{-1}\nabla_h\Box, \phi_0^{n+1}\right), \tag{33}$$

such that

$$-Q_{\rho^{n+1}} R\boldsymbol{G}_{\rho^{n+1/2}} = -(Q_{\rho^{n+1}} R\boldsymbol{G}_{\rho^{n+1/2}})^* + T_{\rho^{n+1}}, \tag{34}$$

where

$$T_{\rho^{n+1}} = [\rho^{n+1}]^{-1}(\nabla_h^2 - \nabla_h \cdot \nabla_h). \tag{35}$$

This procedure is commonly taken to reduce the dimension of the null space, see [36]. Note that the commutator in Eq. (35) is of the order of the spatial discretization accuracy, and introducing the approximate projection does not alter the convergence of the overall method as it is confirmed in § 4.1.

Note that if we allow commutation of the spatial operators in $\boldsymbol{N}_{\rho^{n+1}}$ or use a purely convective discretization, i.e., $\boldsymbol{N}_{\rho^{n+1}} = \boldsymbol{u} \cdot \nabla_h\Box$, then the last three terms in Eq. (32) can be combined into

$$-Q_{\rho^{n+1}} R\boldsymbol{G}_{\rho^{n+1/2}} = -[\rho^{n+1}]^{-1}\nabla_h \cdot \nabla_h + \alpha\nabla_h\phi_0^{n+1} \cdot \nabla_h = -\nabla_h \cdot [\rho^{n+1}]^{-1}\nabla_h, \tag{36}$$

which is the other common form of the pressure-Poisson equation sometimes used in variable-density flows. Subsequently, we will not use this form Eq. (36) owing to the cost of assembly and solution of variable-coefficient Poisson equations and instead prefer the discretely consistent Eq. (33), that uses skew-symmetric discretization, and formulate an iteration that is more efficient. In this work, effort is also made to propose several iterative approaches for this velocity-pressure coupled system Eq. (31). The discussion can be found in Appendix C.

3.3. Solvability considerations

Now, we consider the solvability of Eq. (31) with the approximate projection modification, Eq. (33), which in symbolic form can be written as the linear algebra problem $\mathcal{A}\boldsymbol{x} = \boldsymbol{b}$, where

$$\mathcal{A} = \begin{bmatrix} \boldsymbol{A}_{\rho^{n+1}} & \boldsymbol{G}_{\rho^{n+1/2}} \\ Q_{\rho^{n+1}}\left(\boldsymbol{I} - R\boldsymbol{A}_{\rho^{n+1}}\right) & -(Q_{\rho^{n+1}} R\boldsymbol{G}_{\rho^{n+1/2}})^* \end{bmatrix}, \quad \boldsymbol{x} = \begin{bmatrix} \delta\boldsymbol{z} \\ \hat{p} \end{bmatrix}, \quad \boldsymbol{b} = \begin{bmatrix} 0 \\ -C(\rho^{n+1}\boldsymbol{u}^*, \phi_0^{n+1}) \end{bmatrix}. \tag{37}$$

It is well known that Eq. (37) cannot be uniquely solved for arbitrary $\boldsymbol{b}$ in those situations involving periodic domains or with Neumann pressure boundary conditions; this is not a problem if one disposes of Dirichlet pressure boundary conditions. This happens because the pressure admits a single hydrostatic (constant) mode that belongs to the null space of $\mathcal{A}$; all other spurious pressure modes have been precluded by Eq. (33). This is routinely handled in CFD by either setting the pressure of one point in the domain or the average pressure to a constant. While this works well in constant-density flows, the situation is more difficult in variable-density flow, as we explain now. Before setting the magnitude of the hydrostatic pressure mode, one needs to ensure solvability of the system. The well-known procedure to ensure solvability of Eq. (37) is described by the Fredholm alternative theorem [1] and it involves two parts: first, the enforcement of a solvability condition on $\boldsymbol{b}$ and second, the specification of the magnitude of the hydrostatic mode (typically set to zero). These two steps ensure a unique solution of Eq. (37). Previous approaches remedy the solvability issue by introducing cell-face velocity interpolation or flux splitting to $\boldsymbol{b}$, see [35,34,36]. Despite the lack of a physical interpretation to the modification on $\boldsymbol{b}$, Here, linear algebra theory is used to provide a general solution to the problem. Concretely, one needs to find the null eigenvector $\boldsymbol{w}$ (since there is only one in our case) associated with the adjoint of $\mathcal{A}$, say

$$\boldsymbol{w}^T\mathcal{A} = 0, \quad \text{or} \quad \mathcal{A}^T\boldsymbol{w} = 0, \tag{38}$$

where T superscript denotes transpose, and then enforce that $\boldsymbol{b}$ is orthogonal to $\boldsymbol{w}$, i.e.,

$$\boldsymbol{b}^T \boldsymbol{w} = 0. \tag{39}$$

It is a simple exercise to show that Eq. (39) is ensured by construction in the constant-density flow where $\boldsymbol{w}$ is the constant vector that also equals to the hydrostatic pressure mode because $\mathcal{A}$ is self-adjoint. Unfortunately, $\mathcal{A}$ is not self-adjoint for the variable-density situation and the determination of $\boldsymbol{w}$ is anything but trivial. Removing the part of $\boldsymbol{b}$ that projects onto $\boldsymbol{w}$ is accomplished by

$$\boldsymbol{b} \rightarrow \boldsymbol{b}_w = P(\boldsymbol{w})\boldsymbol{b}, \tag{40}$$

where $P(\boldsymbol{w}) = (I - \boldsymbol{w}\boldsymbol{w}^T)$ and we have assumed that $||\boldsymbol{w}||_2 = 1$; $||\ ||_2$ denotes the Euclidean norm. One then solves $\mathcal{A}\boldsymbol{x} = \boldsymbol{b}_w$ and set the hydrostatic pressure mode to a constant (preferably zero) to obtain a unique solution. This is the second part of the solvability requirement which can be handled by most modern linear algebra packages. Now, we will proceed to the determination of $\boldsymbol{w}$ to show that indeed it is not constant in the variable-density flow.

It is easy to check that the null vector of $\mathcal{A}$ is the constant vector, i.e., the hydrostatic mode. We will now detail the calculation of the null vector of $\mathcal{A}^T$, Eq. (38), and subsequently derive an approximation to highlight that this vector is not constant. Let the null vector of $\mathcal{A}^T$ be denoted by $\boldsymbol{w} = [\boldsymbol{w}_u, w_p]^T$ where we split into velocity and pressure parts $\boldsymbol{w}_u$ and w_p, respectively. Then, Eq. (38) reads

$$\begin{bmatrix} A^T_{\rho^{n+1}} & (I - RA_{\rho^{n+1}})^T Q^T_{\rho^{n+1}} \\ G^T_{\rho^{n+1/2}} & -(Q_{\rho^{n+1}} R \boldsymbol{G}_{\rho^{n+1/2}})^{*T} \end{bmatrix} \begin{bmatrix} \boldsymbol{w}_u \\ w_p \end{bmatrix} = \boldsymbol{0}. \tag{41}$$

Equation 41 can be reduced to a single scalar equation in terms of w_p, by observing that $A_{\rho^{n+1}}$ is not singular, giving

$$\boldsymbol{w}_u = -A^{-T}_{\rho^{n+1}} (I - RA_{\rho^{n+1}})^T Q^T_{\rho^{n+1}} w_p. \tag{42}$$

Then, introduce $\boldsymbol{w}_u$ into the second of Eq. (41) and using Eq. (34) we get, after some rearrangements,

$$w_p^T (Q_{\rho^{n+1}} A^{-1}_{\rho^{n+1}} \boldsymbol{G}_{\rho^{n+1/2}} + T_{\rho^{n+1}}) = 0. \tag{43}$$

The general solution of Eq. (43) depends on the order of discretization, the boundary conditions for the pressure, and the grid and the time step. An explicit general solution is not expected. Nevertheless, we can derive an approximate solution that is accurate for α and Δt asymptotically small by expanding w_p according to

$$w_p = w_0 + \alpha w_\alpha + \Delta t w_\Delta + \mathcal{O}(\alpha^2, \alpha\Delta t, \Delta t^2), \tag{44}$$

and retaining terms to order α and Δt only. The vectors w_0, w_α and w_Δ are to be determined by matching terms of the same order. Expanding $A^{-1}_{\rho^{n+1}}$, ρ^n, R to the first-order, we have

$$A^{-1}_{\rho^{n+1}} = I + \frac{\Delta t}{2Re} \overrightarrow{\nabla}^2_h + \mathcal{O}(\alpha\Delta t, \Delta t^2), \tag{45}$$

$$R = 1 + \mathcal{O}(\alpha\Delta t, \alpha^2), \tag{46}$$

$$\rho^n = \frac{1}{1 - \alpha\phi^n_0} = 1 + \alpha\phi^n_0 + \mathcal{O}(\alpha^2). \tag{47}$$

Substituting the series expansions Eqs. (44)-(47) into Eq. (43) and retaining terms of the corresponding orders, one arrives at

$$\nabla^2_h w_0 = 0, \tag{48}$$

$$\nabla^2_h w_\Delta = -\frac{1}{2Re} \left(\nabla_h \cdot \overrightarrow{\nabla}^2_h \nabla_h \right)^T w_0, \tag{49}$$

$$\nabla^2_h w_\alpha = \frac{1}{2} \left(2[\phi^n]\nabla^2_h + \nabla_h \cdot ([\phi^n]\nabla_h) + \nabla_h \phi^n \cdot \nabla_h - [\phi^n]\nabla_h \cdot \nabla_h \right)^T w_0, \tag{50}$$

where we have used the property that ∇^2_h is self-adjoint. The solution of Eqs. (48)-(49) are w_0 and w_Δ proportional to the constant vector $\mathbb{1} = [1, 1, ...]^T$, while w_α needs to be determined numerically since the source on the right-hand side is not zero in general. Note that we have not assumed that the discrete approximations for spatial derivatives commute in Eqs. (48)-(50). If we had, as if they were continuous operators, one would obtain that the null vector of the adjoint of $\mathcal{A}$ is constant since ∇^2 is self-adjoint and the right-hand side of Eqs. (48)-(50) are all zero. Now, in the discrete non-commutative case, only w_0 and w_Δ are constant, while w_α is not and it depends on ϕ^n. This is important because w_p is needed to enforce Eq. (39) or equivalently to determine $\boldsymbol{b}_w$. In an actual simulation, for finite α and Δt, one should find the null

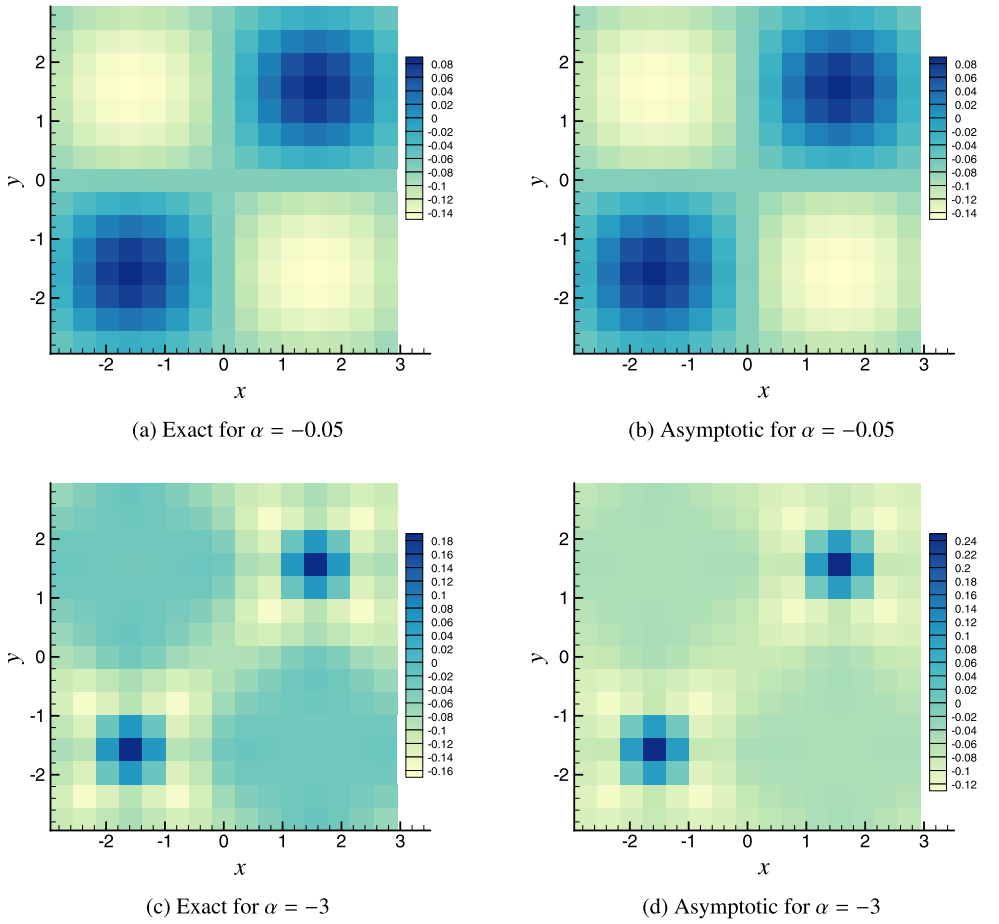

(a) Exact for $\alpha = -0.05$

(b) Asymptotic for $\alpha = -0.05$

(c) Exact for $\alpha = -3$

(d) Asymptotic for $\alpha = -3$

Fig. 1. Exact w_p (left) and asymptotic w_p (right) for $\alpha = -0.05$ (top) and $\alpha = -3$ (bottom) on a mesh of 16x16 grid points. (For interpretation of the colors in the figure(s), the reader is referred to the web version of this article.)

vector of the transpose of $\mathcal{A}$ from Eq. (41) (at each time step). Note that one only needs w_p since $\boldsymbol{w}_u$ is always zero but it is undesirable to use Eq. (43) because it requires the inverse of $A_{\rho^{n+1}}$. The preferred approach is to solve a linear system using Eq. (38) directly by setting one element of w_p to a constant and moving that element to the right-hand side; after the solution is found, the vector can be normalized. This is possible because we know that the dimension of the null space is exactly one.

We will show in later examples some typical w_p and also highlight that it is very important to enforce solvability to ensure convergence of the iterative method used to solve Eq. (37). We observe that the convergence rate of the iterative linear solver stalls if the solvability condition is not enforced. In this state, the solution returned by the linear solver may be the least-square solution, which is the same as that obtained when enforcing the solvability condition, but at a much higher computational cost. However, if the iterative linear solver quits too soon, and the least-square solution is not reached, the simulation can become quickly unstable. We speculate that most problems observed in variable-density solvers at sufficiently high density ratios are a consequence of the attempt to solve the singular Eq. (37) without paying attention to the solvability condition. Finally, note that these problems do not arise in the pseudo-spectral method, since the spatial commutation properties can be applied and w_p is constant, which is consistent with the observation that spectral codes for variable-density flows work relatively well.

Fig. 1 shows a comparison of the vectors w_p obtained exactly (left column) and asymptotically (right column) for two values of α: -0.05 and -3. The scalar ϕ_0 is the manufactured solution described in § 4. The grid size is set to 16×16 and $\Delta t = 10^{-4}$ for the exact vector. The constant component of the exact w_p is removed from the figures to aid the comparisons. We observe that the asymptotic approximation is very close to the exact null vector for small α and it necessarily deviates for larger magnitudes of α; although it retains the qualitative features of the vector.

4. Numerical experiments

Here, we evaluate some of the quantities discussed previously using a manufactured solution problem in two dimensions that can be controlled carefully. The focus is on demonstration of some of the numerical properties of the discrete

variable-density equations discussed in § 3. Unlike the constant-density problem, the manufactured solution to the variable-density zero-Mach Navier-Stokes equations cannot be chosen arbitrarily because the mass constraint relates the temperature, density, and velocity among themselves. The manufactured solution serves as a benchmark in the code verification for convergence rates and mass conservation in § 4.1. Nonlinear stability is assessed subsequently in § 4.2 with a different forced variable-density mixing problem; more suitable for long time integration. These tests are chosen to provide some guidelines representative of actual applications but we should keep in mind that all results in this section are problem-dependent. It is very difficult to establish results of general validity in non-solenoidal variable-density flow owing to the strong coupling (nonlinearity) of the equations.

4.1. Convergence study

The first test uses the manufactured solution given by

$$u(x,y,t) = \frac{1}{\rho}\cos(x)\sin(y)H(t) + \frac{1}{\rho}\cos(x)\sin(y)Q(t), \tag{51}$$

$$v(x,y,t) = \frac{1}{\rho}\sin(x)\cos(y)H(t) - \frac{1}{\rho}\sin(x)\cos(y)Q(t), \tag{52}$$

$$p(x,y,t) = -\cos(x)\cos(y)Q(t), \tag{53}$$

where

$$H(t) = \frac{\omega}{4}(\rho_{\max} - \rho_{\min})\sin(\omega t), \quad Q(t) = \cos(\omega t),$$

in a two-dimensional periodic domain $[0, 2\pi]^2$. As emphasized in the previous discussion, the mass constraint should be satisfied initially to ensure consistency of the fields at later times. Therefore, the scalar field needs to be compatible with the above manufactured hydrodynamic fields. Substituting the manufactured velocity fields into the continuity equation, Eq. (1), leads to a differential equation for the density, given by

$$\frac{\partial \rho}{\partial t} - 2\sin(x)\sin(y)H(t) = 0, \tag{54}$$

which has the solution

$$\rho(x,y,t) = \frac{\rho_{\max} - \rho_{\min}}{2}\sin(x)\sin(y)\cos(\omega t) + \frac{\rho_{\max} + \rho_{\min}}{2}, \tag{55}$$

where the integration constant is chosen to set the density in the range between $\rho_{\min}$ and $\rho_{\max}$. Finally, the scalar field is determined from the SR, Eq. (7). This manufactured solution is periodic in both space and time and suitable for the numerical assessment below. The source terms that correspond to these manufactured fields are not reported for sake of space but they can be calculated explicitly from Eqs. (51)-(55).

The convergence study is carried out for $\alpha = -3$, which corresponds to a density ratio $r = \rho_{\max}/\rho_{\min} = 4$, $\omega = 2\pi$, $Re = 100$, and $Pe = 100$. The spatial accuracy of the finite-difference discretization is tested by fixing $\Delta t = 10^{-4}$ and integrating all fields for one period. The mesh is refined successively from 16×16, 32×32, 64×64, to 128×128 grid points, and the global spatial errors are calculated with the known manufactured solutions and presented in terms of the L_2 norm. Bootstrapping with explicit Euler is used in the first three iterations, at the corresponding smaller time steps, since the Adams-Bashforth time integrator cannot self-start. In this section, the linear systems of equations, Eq. (37), are always solved using classical GMRES with a Krylov subspace dimension that is sufficiently large in order to avoid restarts.

Fig. 2 show the spatial convergence rates for the 2nd, 4th, 6th order finite-difference discretization and the pseudo-spectral method. The reference orders of accuracy are plotted in black solid lines in these plots. It is observed that all fields converge at the expected rate for each discretization. The pseudo-spectral discretization converges to the threshold set by the time integration method, of the order of 10^{-6} for velocity, except for the coarse 16×16 grid where we do not have sufficient grid points to resolve the solution well. Note that pressure has a higher error in all cases but still converges at the correct rate while the smallest error is observed in the temperature, ϕ_0.

The temporal order of accuracy is shown in Fig. 3 for a mesh with 64×64 grid points and using the 2nd and 4th order finite-difference discretization (similar results are obtained for the other spatial discretizations we consider). It is observed that the temporal error for all the variables converges at a rate of $\mathcal{O}(\Delta t^2)$ uniformly when the time-step size decreases from 0.1, 0.05, 0.025, to 0.0125. This order of accuracy verifies the implementation of the second order AB/CN time integrator as well as the pressure projection approximation.

Finally, an assessment of mass conservation is carried out on a mesh using 64×64 grid points, 4th-order spatial discretization, and time-step sizes: $\Delta t = 10^{-2}$, 5×10^{-3}, 2.5×10^{-3}, and 1.25×10^{-4} corresponding to initial CFL numbers of 0.8, 0.4, 0.2, and 0.1, respectively. The total mass is defined by $M = \sum_{i,j} \rho(x_i, y_i)\Delta x \Delta y$. Fig. 4 shows that M converges at a rate of $\mathcal{O}(\Delta t^2)$, which is the same as the order-of-accuracy of the AB/CN time-integrator, as expected. Fig. 4 includes the time history of the scaled total mass errors, $\frac{M(t)-M_0}{M_0\ \mathrm{CFL}^2}$, where M_0 is the total mass at $t = 0$ (observe that CFL contains

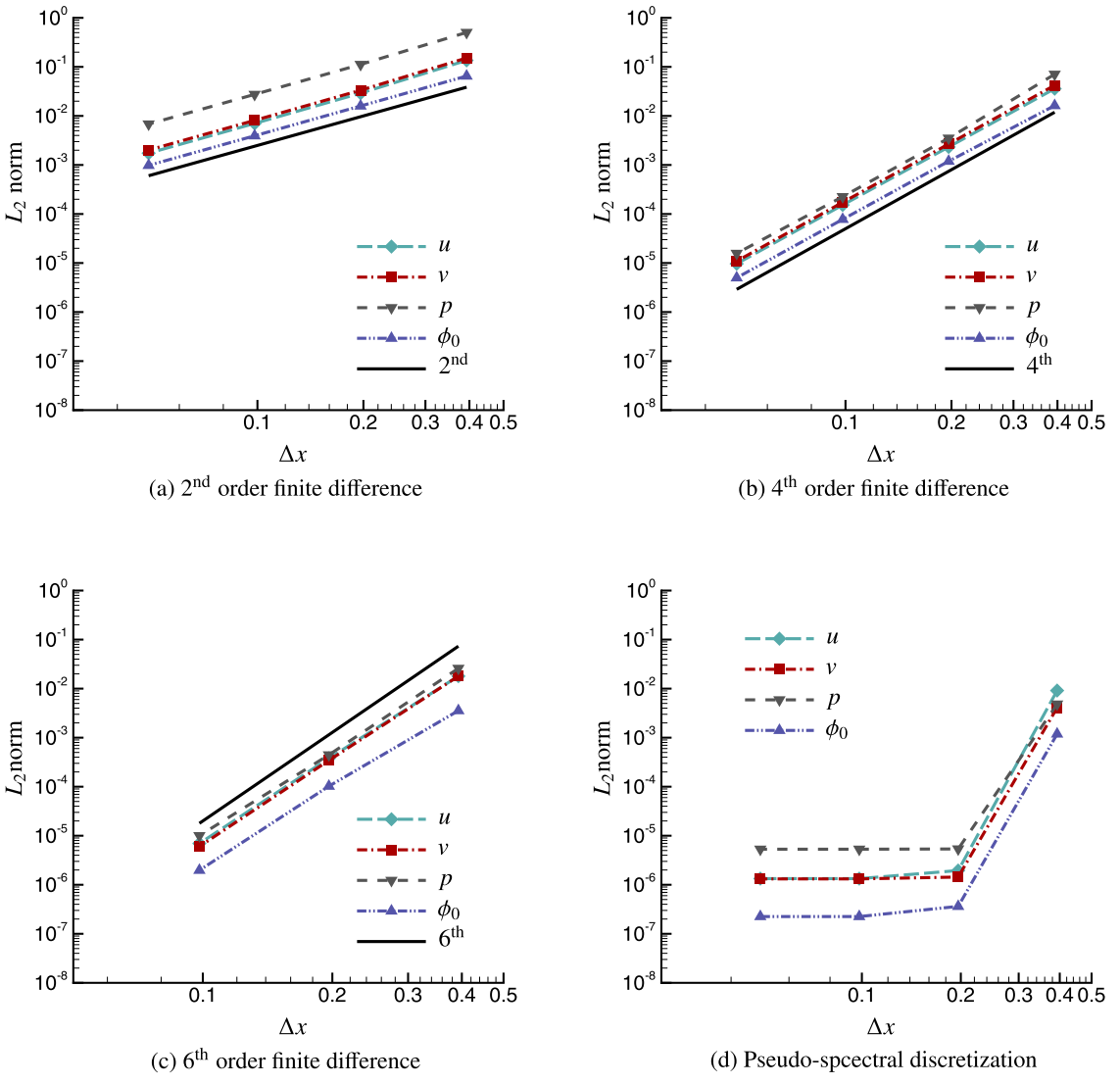

(a) 2^{nd} order finite difference

(b) 4^{th} order finite difference

(c) 6^{th} order finite difference

(d) Pseudo-spcectral discretization

Fig. 2. Spatial convergence study for 2nd (a), 4th (b), 6th (c), and pseudo spectral (d) order of accuracy.

Δt). Because the convergence tests are carried out in the same grid and same manufactured solution, the scaling factor for the total mass errors is solely controlled by the refinement of Δt. When the total mass errors are scaled by Δt^2, all curves in Fig. 4 collapse into one, indicating the second order convergence in time. Note that if the approximate pressure projection method is working correctly, the total mass must converge at the same rate as the temperature, which is shown previously to be also second-order accurate in time. Fig. 5 shows also the total mass variation using a fixed time-step size ($\Delta t = 5 \times 10^{-3}$) and different spatial discretizations and grid sizes. It is clearly seen that the total mass variation (owing to the approximate projection nature of the algorithm) is exclusively controlled by the time integrator (order and step size) and not by the order of the spatial discretization error or the mesh size. This highlights that the approximate projection method has desirable properties and that the commutation error, Eq. (35), is not a controlling factor as long as it is of higher order than that of the temporal integrator.

4.2. Nonlinear stability assessment

The stability of a numerical scheme for the variable-density flows in the zero-Mach limit could degrade as the density variation increases. Numerical simulations can only be performed with a significantly small time step size which offsets the performance gain compared to the fully compressible equations; this finding is largely based on perusal of published simulations. This is further complicated by the observation that the difficulty seems to be on the nonlinearity induced in the equations by the varying density. It is believed that a discrete scheme is more likely to trigger the onset of numerical stabilities when it is designed to sacrifice temporal convergence in exchange for the solvable pressure in the variable density

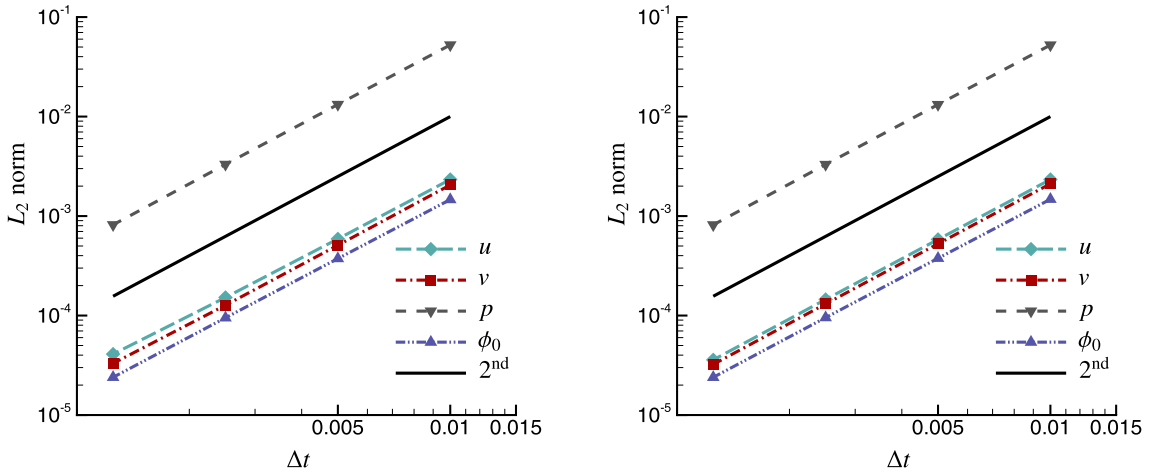

Fig. 3. Temporal convergence of 2nd order AB/CN using 2nd and 4th order spatial finite differences on a mesh with 64×64 grid points.

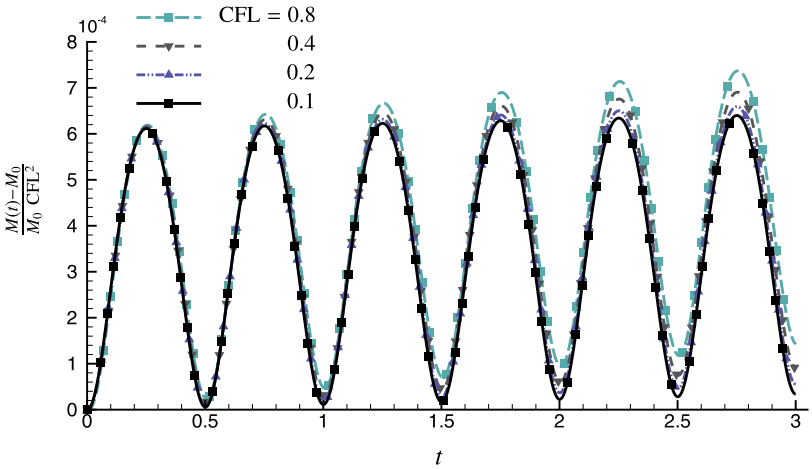

Fig. 4. Total mass error scaled by Δt^2 for the fixed mesh of 64×64 grid points for 4th-order spatial discretization.

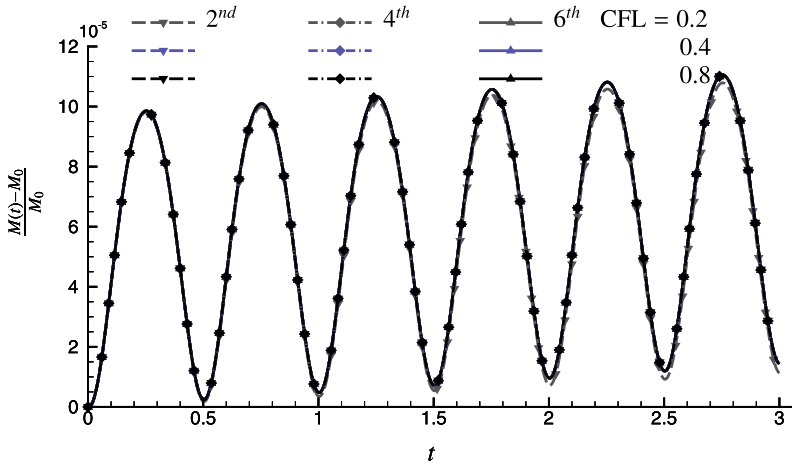

Fig. 5. Total mass error with different spatial discretizations and grids for constant $\Delta t = 5 \times 10^{-3}$. Dash, dotted dash, and solid lines correspond to 2nd, 4th, and 6th order finite-difference methods, respectively. The different colors represent different CFL numbers or grid size (32×32, 64×64, 128×128).

flows. As shown in the convergence studies, the proposed numerical method converges all variables at a uniform order of accuracy which should in principle enhance the numerical stability to some extent. Studying stability by linearizing the equations is not always practical, and seldom of sufficient generality since the result depends on the base density field about which stability is analyzed. Therefore, we assess nonlinear stability with a forced variable-density flow with initial conditions defined by

$$u(x,y) = \cos(x)\sin(y), \quad v(x,y) = -\sin(x)\cos(y), \quad \phi_0(x,y) = \frac{1}{2}\left(1+\sin(x)\sin(y)\right), \tag{56}$$

while the time-dependent force and source terms that maintain the motion of the flow are given by

$$f_x(x,y,t) = 2\cos(x)\cos(y)\sin(\pi t), \quad f_y(x,y,t) = 2\sin(x)\sin(y)\sin(\pi t), \tag{57}$$

$$\varpi(x,y,t) = \frac{0.4}{\sqrt{r}}(0.5+0.5\tanh(t-2))\cos(x)\sin(y)\sin(\pi t). \tag{58}$$

We integrate the equations for a long time at several Reynolds numbers with the Peclet number fixed at 200 using all previous spatial discretizations: 2nd, 4th, 6th, and pseudo-spectral on a mesh with 32×32 grid points. It is difficult in this problem to compute the errors of all variables and determine precisely where the onset of numerical instability takes place since the exact solution to this variable-density Navier-Stokes flow is not known. Nonetheless, it is expected that the fields and kinetic energy should remain within a reasonable range if the flow is stable. Therefore, we use the following procedure to monitor the simulations and determine if the solution shows any indication of numerical instability by:

(1) for a given cell Reynolds number, defined by

$$Re_{\text{cell}} = Re\frac{\rho_{\min}(|u|_{\max}/\Delta x + |v|_{\max}/\Delta y)}{(1/\Delta x^2 + 1/\Delta y^2)},$$

and density ratio, attempt the numerical integration with a fixed time-step size Δt,
(2) if the kinetic energy exceed 10 times the initial value, we consider the flow to be unstable and the program aborts and restarts the test with a smaller Δt,
(3) if the temperature maximum and minimum exceed their expected limits by more than %2, the program aborts and restarts the test with a smaller Δt,
(4) continue this procedure until all cell Reynolds numbers and density ratios are explored.

These stopping criteria capture most of the numerically unstable situations correctly. Fig. 6 shows sample results from simulations on a mesh of 32×32 grid points using the 4th order finite-difference method. The flow parameters correspond to $\frac{\rho_{max}}{\rho_{min}} = 4$, and $Re_{\text{cell}} = 25,\ 50,\ 100$. Note that one should not infer that higher cell Reynolds number should become unstable earlier because in these nonlinear stability tests the time step is being changed differently in each simulation to detect the onset of instability; Re_{cell} is independent of time step.

Nonlinear stability curves shown as maximum CFL number as a function of cell Reynolds number, $Re_{\text{cell}}(t=0)$, and density ratio, r, are shown in Fig. 7 for this test problem. It is observed that the maximum CFL number that can be stably maintained decreases somewhat as the order of accuracy of the spatial discretization increases, owing to the better modified wavenumber behavior, as expected. This is observed also in linear problems, with the pseudo-spectral method requiring the most stringent time step restriction for a given time integration method. The figure also shows that the maximum CFL decreases with increasing density ratio owing to stronger variable-density nonlinearity. This happens uniformly for all spatial discretization orders. The 6th order spatial discretization shows a slightly larger limit at $r = 15$ and $Re_{cell} = 100$, which we attribute to the discrete nature of the stopping criterion. The result is still monotonic with increasing r but somewhat higher than visual inspection would suggest. Note the 2nd order case shows similar behavior but not as pronounced. The tests are shown up to $r = 20$, although higher density ratios are possible (not reported) with the subsequent decrease of maximum CFL, because that is a practical upper limit for typical miscible or combustible fluids; obviously immiscible fluids can have much larger density ratios.

4.3. Consequences of enforcing the solvability requirement

Here, we consider in more detail the effect of enforcing the solvability condition, discussed in § 3.3, on the pressure-velocity system, Eq. (37). As before, we consider the iterative solution using GMRES when the solvability condition is enforced, Eq. (40), and also when it is not enforced. In the latter case, GMRES can generate a solution that is optimal in a least-square sense, where the residual $\|\mathcal{A}\boldsymbol{x} - \boldsymbol{b}\|_2$ saturates prematurely to a constant value and cannot be decreased further. We investigate the behavior of the residual in the iterative linear solver using meshes with 16×16, 32×32, and 64×64 grid points with $\Delta t = 0.01$ and 4th order finite-difference discretization (similar results are obtained for the other orders of spacial accuracy).

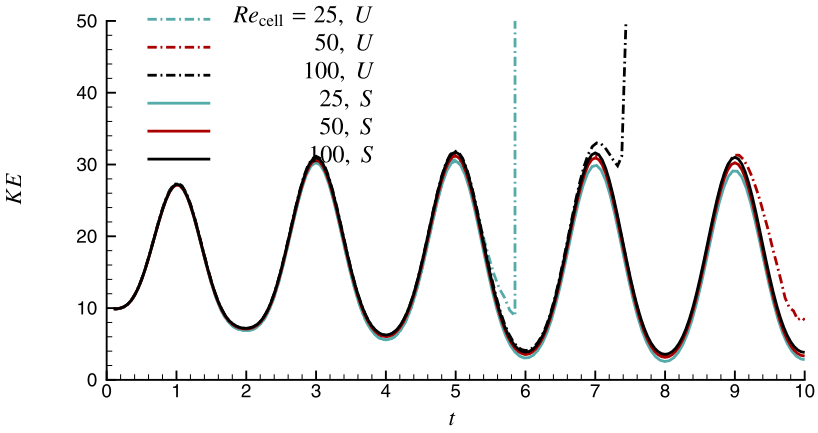

(a) Kinetic energy

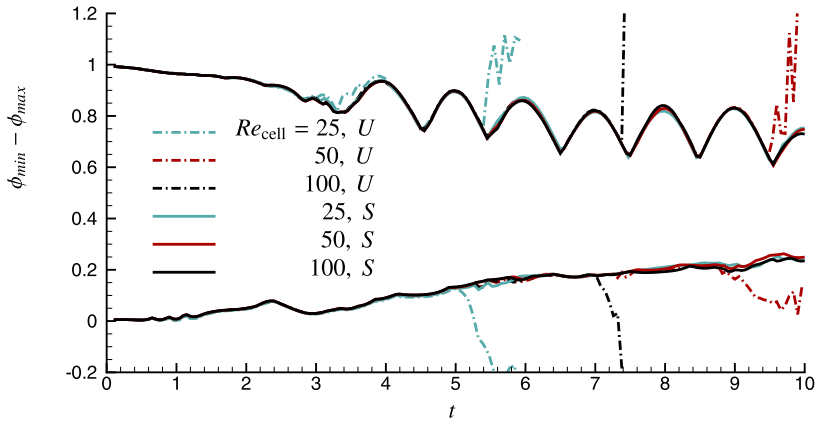

(b) Minimum and maximum values of temperature

Fig. 6. Examples of stable (S) and unstable (U) nonlinear numerical tests.

Fig. 8 and Fig. 9 show the evolution of the residual in the iterative linear solver during the first time step using the manufactured solution, § 4.1, and the variable-density mixing problem, § 4.2, respectively. In these plots, the horizontal axis is the iteration number l of the GMRES solver. One observes that the residuals of Eq. (37) stall after about 50, 100, and 200, iterations for the 16×16, 32×32, and 64×64 meshes, respectively. The final magnitude of the residual is connected with the order of spatial discretization, and reaches around 10^{-3}, 10^{-5} and 10^{-7} for the previous meshes, respectively, if the solvability condition is not enforced. The same figures show how the residual keeps decreasing if the solvability condition is enforced from the outset. Note that the residuals are identical before saturation when the solvability condition is not enforced. The level at which the residual saturates in the GMRES iteration can be determined from our previous analysis. The residual of the linear system $\|\mathcal{A}\boldsymbol{x} - b\|_2$ can be expanded as

$$\|\mathcal{A}\boldsymbol{x} - \boldsymbol{b}\|_2 = \|\mathcal{A}\boldsymbol{x} - \boldsymbol{b}_w + \boldsymbol{b}_w - \boldsymbol{b}\|_2 = \|\boldsymbol{w}(\boldsymbol{w}^T\boldsymbol{b})\|_2 = \left|\boldsymbol{w}^T\boldsymbol{b}\right|, \tag{59}$$

where we have used the orthogonality of $\mathcal{A}\boldsymbol{x} - \boldsymbol{b}_w$ and $\boldsymbol{b}_w - \boldsymbol{b}$. Fig. 8 and Fig. 9 show as thick horizontal lines over the saturation region the values of $\left|\boldsymbol{w}^T\boldsymbol{b}\right|$, which evidently match. For completeness, the figures also show the initial null vector w_p for these two cases on the left-hand side. These figures are illustrative of an important behavior that one should be aware. First, one cannot solve the linear system of equations associated with the pressure by a direct linear solver or one relying on the existence of an exact (to within machine accuracy) solution of the equations if the solvability condition is not enforced explicitly. Second, conjugate-gradient or its generalization based on Krylov-space methods will produce a (least-squares) solution but only after the iteration stopping criterion is reached. This can represent a substantial waste of computational time since all iterations performed after saturation of the residual are useless. Third, choosing a loose residual tolerance to induce early termination of the iteration is also not reliable because residual saturation depends on the order of the numerical method and the size of the mesh. Therefore, in conclusion, the computational cost savings gained by enforcing the solvability condition can vary between zero, if one so happens to chose a tolerance just before the saturation

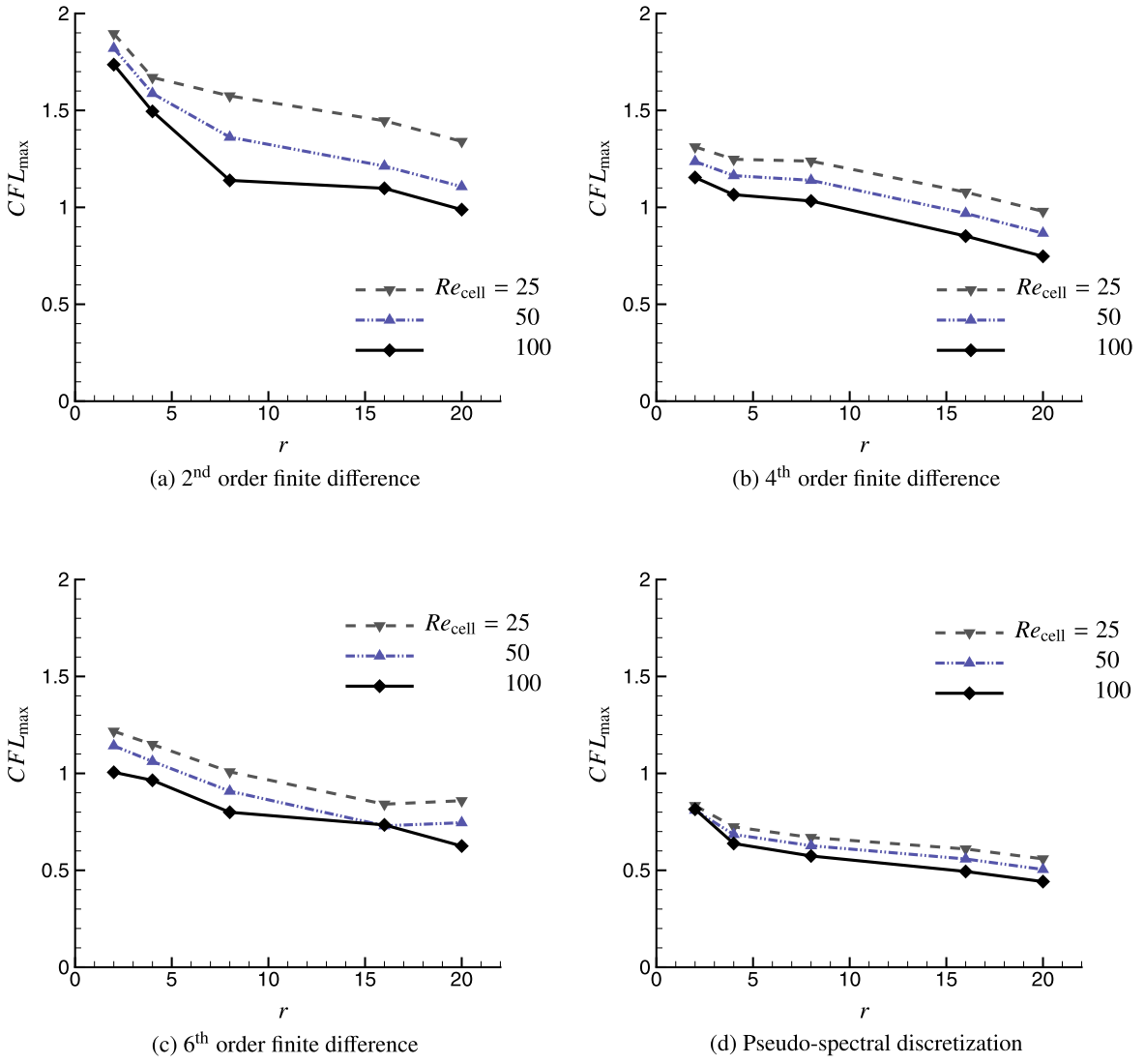

Fig. 7. Maximum CFL attainable as a function of cell Reynolds number and density ratio for different spatial discretizations.

of the residual error, to essentially infinite if the tolerance is below the saturation point. In other terms, if the tolerance of the iterative linear solver is chosen below 10^{-7} in Fig. 8 and Fig. 9, the computational cost is infinite, only limited by the maximum number of linear iterations chosen, not by a convergence criterion.

The inner product of the null-vector and the right hand side vector of pressure equation $\boldsymbol{w}^T\boldsymbol{b}$ decrease as one refines the grid spacing Δx and time-step size Δt. Fig. 10 shows $\boldsymbol{w}^T\boldsymbol{b}$ when integrating the manufactured solution for the first time-step using different discretization and grids. It is observed that the magnitude of this correction term decreases at approximately the same rate as the order of the spatial error. Manufactured solutions are also integrated for one period of time with different Δt on a 64×64 mesh using 4th order finite-difference method. As shown in the right plot of Fig. 10, $\boldsymbol{w}^T\boldsymbol{b}$ varies as density ratios change but it converges in time at a faster rate (approximately 3^{rd} order) than the time integration scheme. This indicates that correcting $\boldsymbol{b}$ by enforcing the solvability constraint does not impact the order-of-accuracy of the overall method; which is a consequence of consistency of the overall discretization.

Finally, Fig. 11 shows temporal convergence tests using 2nd order finite-difference spatial discretization, without enforcing the solvability condition, when setting the maximum number of iterations in GMRES to 20 and 40 iterations (arbitrary but not unusual numbers for this small problem). One finds that the temporal convergence rate is not affected if the linear solver is allowed to find the least-square solution, here needing more than 200 iterations, and the results are indistinguishable from those in Fig. 3. On the other hand, if the solver is configured to perform a reduced number of iterations, then the temporal convergence rate is affected. It is observed that with only 20 iterations all fields are first-order accurate in time except the pressure that is zeroth-order accurate. Using 40 iterations reproduces the second-order temporal accuracy for all fields except the pressure that converges at a lower order. As well known, the pressure is a set of Lagrangian multipliers if

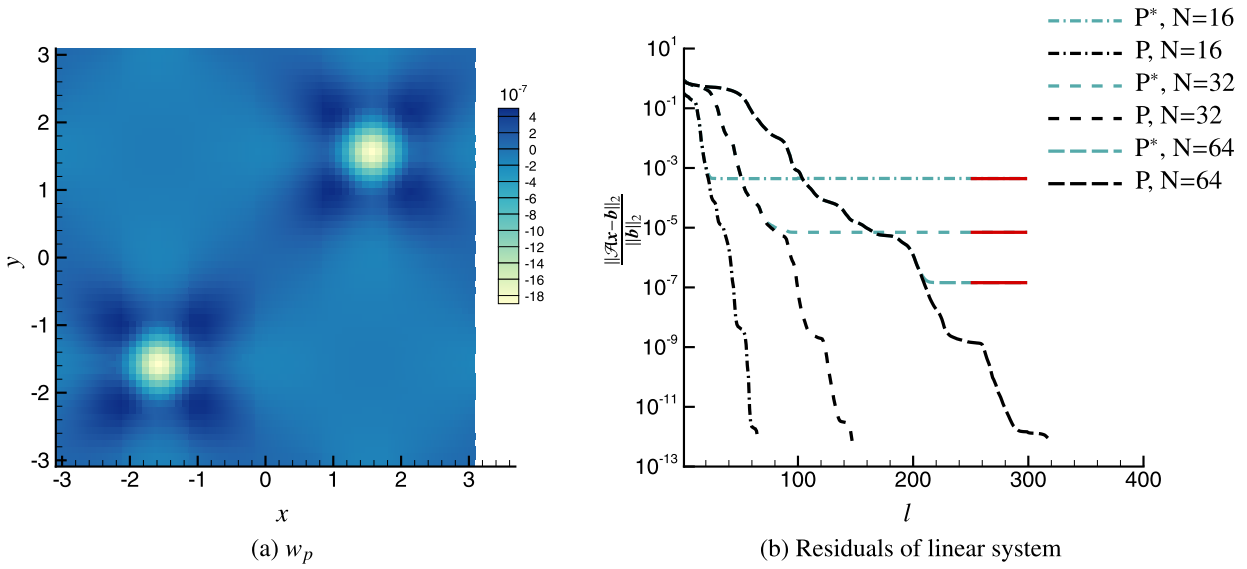

(a) w_p (b) Residuals of linear system

Fig. 8. Null-vector of the manufactured solution (left) and the effect of solvability enforcement (or not) on linear solver convergence (right) for § 4.1. P* and P denotes periodic problem with solvability not enforced and enforced, respectively.

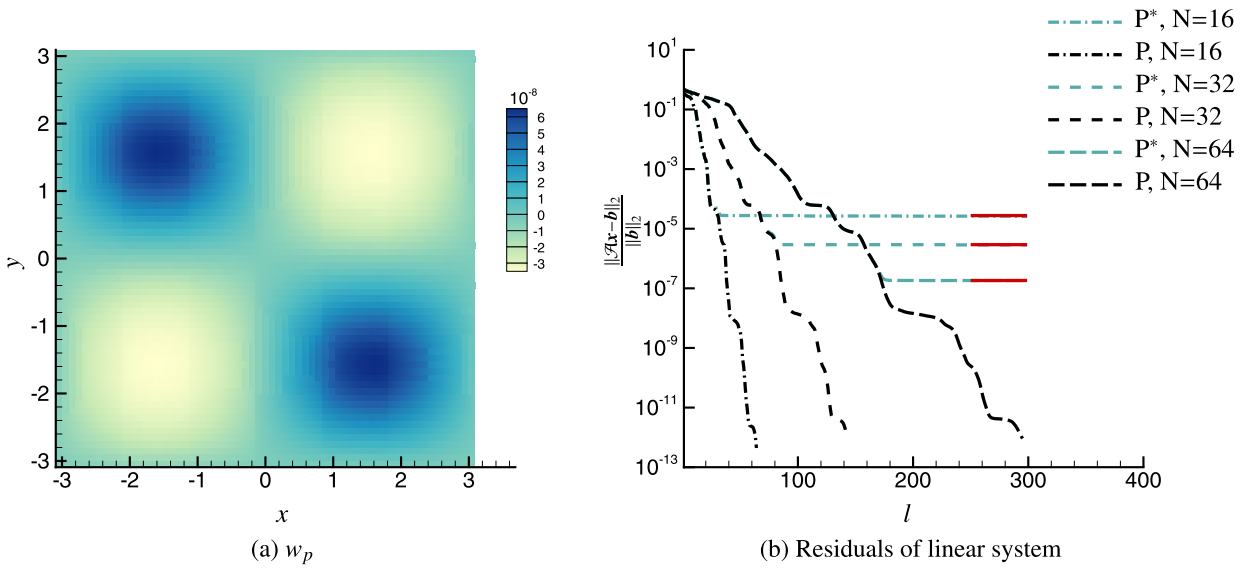

(a) w_p (b) Residuals of linear system

Fig. 9. Null-vector of the variable-density mixing problem (left) and the effect of solvability enforcement (or not) on linear solver convergence (right) for § 4.2. P* and P denotes periodic problem with solvability not enforced and enforced, respectively.

one casts the equation Eq. (31) into the Karush-Kuhn-Tucker system. The pressure does not directly involve in time advancement but is responsible to minimize the residual of the mass constraint. Therefore, despite that the pressure convergence is degraded, other flow fields are still converge at a specified order of accuracy. The purpose of this paper is to report one approach ensuring the convergence of the pressure and avoiding the situation Fig. 3(b) to happen.

5. Numerical simulations

In this section, we showcase the capabilities of the numerical solver. It is shown that the proposed numerical method can be easily extended to include buoyancy effects, chemical reactions, inflow/outflow boundaries and that the method is indeed applicable for large-scale 3D simulations.

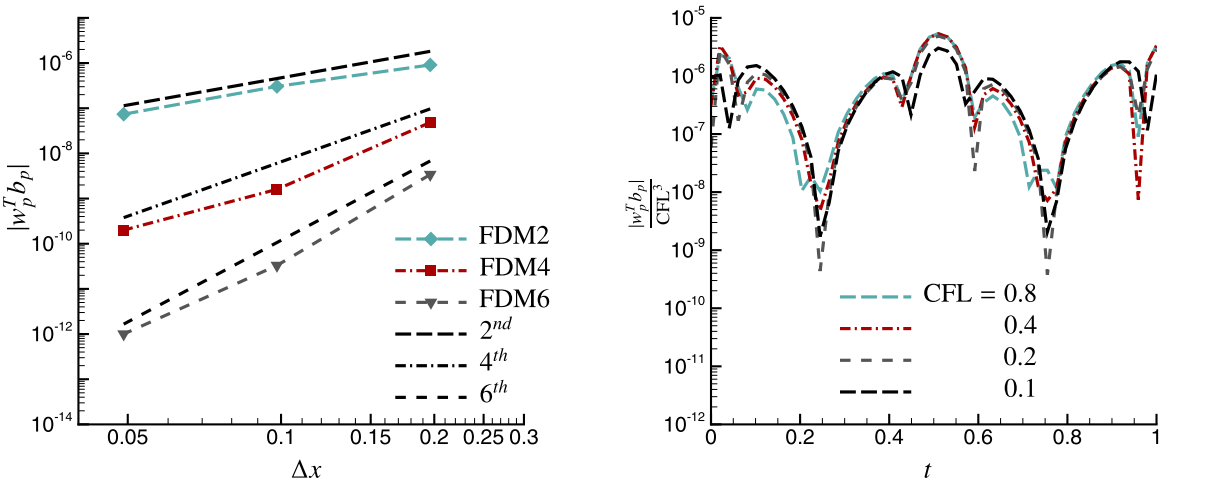

(a) $|w_p^T b_p|$ using different discretizations (b) $|w_p^T b_p|$ scaled by CFL^3 over one period using different Δt

Fig. 10. Comparison of $w_p^T b_p$ using different Δx (left) and Δt (right).

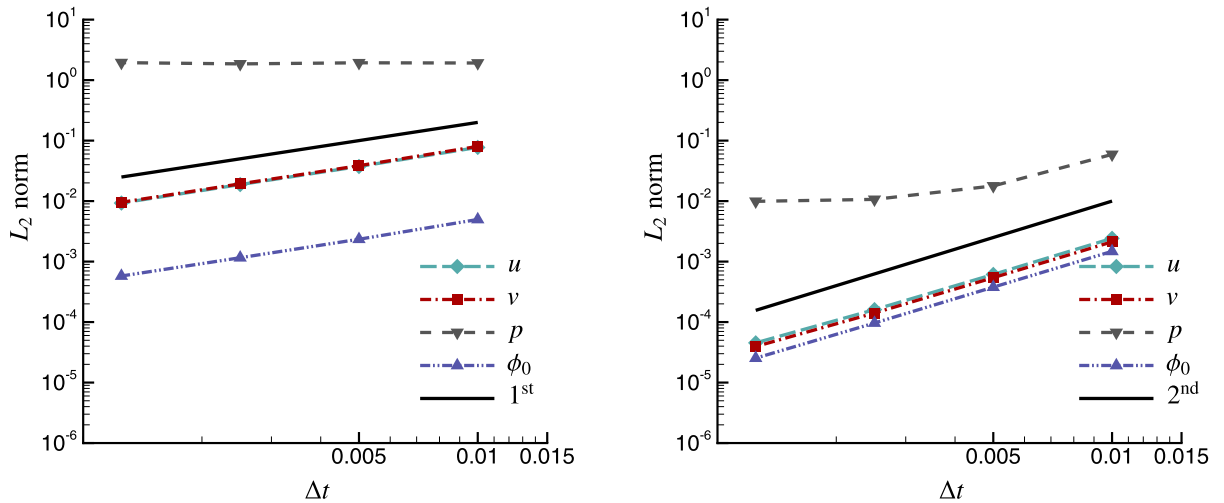

(a) 20 GMRES iterations (b) 40 GMRES iterations

Fig. 11. Effects of not enforcing the solvability condition on the temporal convergence for 2nd order spatial discretization.

5.1. Two-dimensional Reyleigh-Taylor flow

The interface between two fluids of different densities subject to a constant background body force (gravity) is known to exhibit the so-called Rayleigh-Taylor instability (RTI) when the fluid above is heavier than the fluid below. It is one of the important canonical applications of the zero-Mach Navier-Stokes equations; see [19,52,53,9,11,24,54,16,42]. In this section, we compare with published results [9] and consider a 2D domain of size $L_x = 1$ and $L_y = 4$ that is discretized by a mesh of 200×800 grid points using the 4th order finite-difference method. Gravity ($\boldsymbol{f} = [0, -1]^T$) points downward along the y direction. The flow is periodic in its transverse direction and no-slip boundary conditions are enforced at $y = \pm\frac{1}{2}L_y$ while the pressure employs the Neumann-type condition $\frac{\partial p}{\partial n} = \rho \boldsymbol{f}$, where n denotes the normal direction to the boundary. The initial density is given by

$$\rho(x, y, 0) = \frac{\rho_{max} + \rho_{min}}{2} + \frac{\rho_{max} - \rho_{min}}{2} \tanh\left(\frac{y - 0.1\cos(2\pi x/L_x)}{h}\right), \tag{60}$$

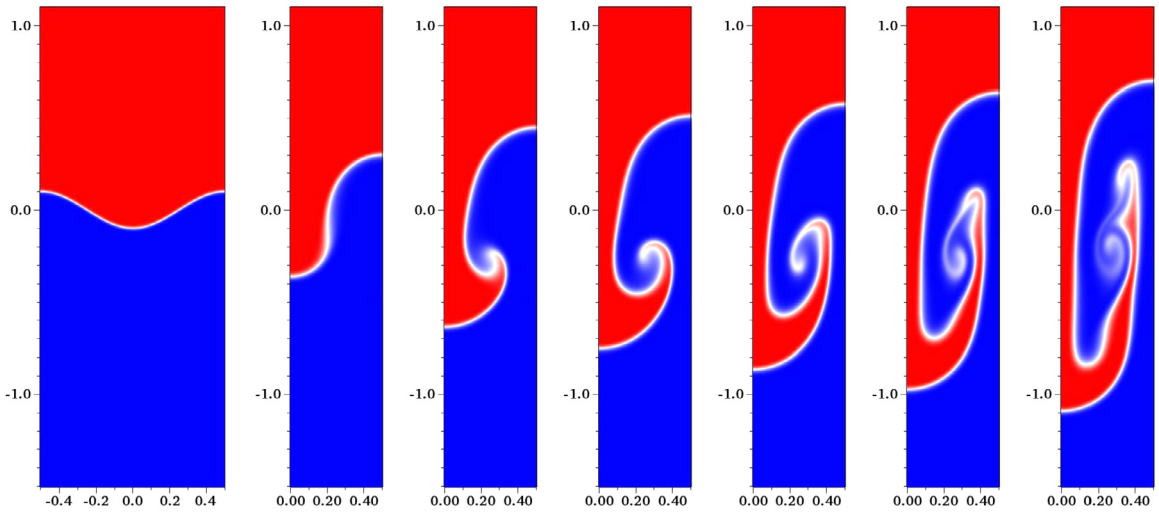

(a) $At = 0.5$

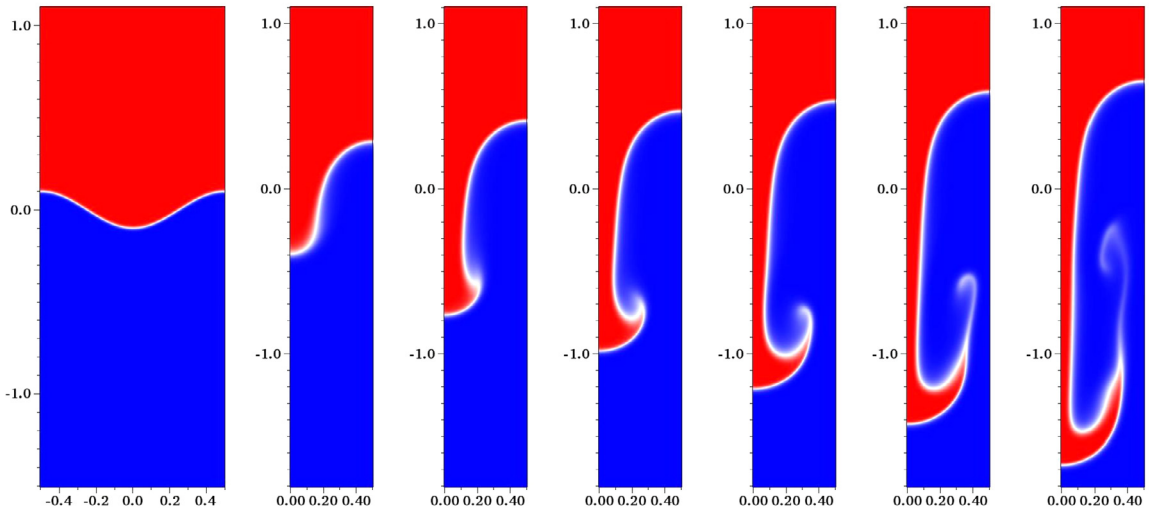

(b) $At = 0.85$

Fig. 12. Density contour plots of RTI at $t = 0$, $1/\sqrt{At}$, $1.5/\sqrt{At}$, $1.75/\sqrt{At}$, $2/\sqrt{At}$, $2.25/\sqrt{At}$, and $2.5/\sqrt{At}$ (from left to right respectively).

where h is the thickness of initial density layer. The maximum density ρ_{max} and the minimum density ρ_{min} define the Atwood number, which is provided by

$$At = \frac{\rho_{max} - \rho_{min}}{\rho_{max} + \rho_{min}}.$$

The first test sets $\rho_{max} = 1$, $\rho_{min} = 1/3$, and $h = 0.01L_x$. The Reynolds number and Schmidt number (the ratio between viscous diffusion rate and mass diffusion rate) are set to $Re = 1000$ and $Sc = 2$. This choice of parameters is the same as that in [9]; note that study considers divergence-free flow and advects the density itself instead of species concentration or temperature as in the present case. Furthermore, there is no Schmidt or Prandtl number defined there. Nonetheless, numerical solutions Fig. 12a at $t \approx 1/\sqrt{At}$, $1.5/\sqrt{At}$, and $1.75/\sqrt{At}$ match well those reported in [9]. The late-time solutions (beyond $t \approx 2/\sqrt{At}$) differ slightly, because of the treatment of mass diffusion, where [9] used artificial non-linear viscosity for numerical stability, see [55], but we employ the physical diffusion.

Using the same mesh and flow parameters, the second testing case increases the density ratio to 12.5, that is, $\rho_{max} = 1$, $\rho_{min} = 0.08$, and $At = 0.85$ and the initial density layer thickness $h = 0.04L_x$. Numerical solutions Fig. 12b show that the heavy fluid above moves downward at a faster rate and a longer "spike" is formed. The inertial effect dominates the fluid motion and the development of shear-induces vortices is slower compared to the low density ratio case.

5.2. Freely propagating premixed flames

Here, we consider a two-dimensional freely propagating premixed flame subject to incoming flow forcing. The flame propagates vertically, along the y direction, and it is periodic along the x direction. The domain size is $L_x = 12$ and $L_y = 32$ with a mesh of 192×512 grid points. The flow is first initialized with a steady-state laminar planar premixed flame solution and perturbed sinusoidally. The laminar one-dimensional premixed flame solution is calculated with higher numerical accuracy using a one-step reaction chemistry model with reaction rate of Arrhenius type, provided by

$$\varpi = \mathrm{Da}\rho\phi_1 \exp\left(-\frac{\alpha\phi_{0,a} - 1}{\alpha\phi_0 - 1}\right), \tag{61}$$

where Da denotes the Damköhler number, the reduced temperature is $\phi_0 = \frac{T - T_u}{T_b - T_u}$ (T, T_u, and T_b represent the local, unburned side, and burned side temperatures, respectively), where $\phi_{0,a}$ denotes the reduced activation temperature, and ϕ_1 is the mass concentration of reactant. Using these scaling, one can deduce $\alpha = -\frac{T_b - T_u}{T_u}$.

At the inlet, synthetic isotropic quasi-turbulent velocity perturbations are convected into the domain at a dynamically adjusted mean flow speed to maintain the mean position of the flame within the domain. Dirichlet velocity boundary conditions are used at the inflow where $u = \tilde{u}$ and $v = s_f + \tilde{v}$; $\tilde{u}$ and $\tilde{v}$ denote the velocity fluctuations and s_f is the mean flame speed. The energy spectrum of the velocity fluctuations is given by

$$E(k; u', \mathcal{L}) = u'^2 \frac{32}{(2\pi)^{11/2}} (k\mathcal{L})^4 \exp\left(-\frac{k^2\mathcal{L}^2}{2\pi^2}\right), \tag{62}$$

where $\mathcal{L} = 2$ is the turbulence integral length-scale, u' is the root-mean-square of velocity fluctuation and k denotes wavenumber $k_j = \frac{2\pi}{L} j$ with $j \in \mathbb{Z}$, . The flow parameters are $Re = 180$, $Pe_0 = 1.82$, and $Pe_1 = 1.82$, velocity intensity $u'/s_L = 0.5$, thermal expansion $\alpha = -1.82$, and Damköhler number $\mathrm{Da} = 128,000$. The mean inflow speed s_f is dynamically adjusted by a closed-loop PID controller that maintains the flame position, defined by

$$\bar{y}_f = \frac{\int \varpi\, y dV}{\int \varpi\, dV}, \tag{63}$$

at a nominally fixed location $y_f^o = -2$.

Fig. 13a shows a snapshot of the vorticity field and flame profile after the stationary state is achieved. The parameters chosen for this flame situate it in the wrinkled flamelet regime, similar to results reported by [56]. Here, the flame surface continuously experiences external flow perturbations that induce flame deformations, but the flame retains a structure that is mostly like that predicted by asymptotic techniques. The figure also shows the laminarization of the flow after it traverses the flame, since the density is smaller (lower Reynolds number) and viscous decay consumes most the small scale vorticity that comes across the flame. Fig. 13b shows multiple instantaneous flame profiles over time to highlight the unsteady nature of the flow and the characteristic thickness of the flame brush. Fig. 13c shows the mean location of the flame as a function of time, where the stabilization of the flame at about y_f^o is clearly seen.

5.3. Isotropic turbulent flow

Finally, one three-dimensional direct numerical simulation of variable-density turbulence subject to stationary isotropic forcing of momentum and temperature was carried out to showcase that the issues discussed previously in two dimensions can also be addressed in three dimension. The forcing is chosen to ensure statistical stationary conditions. The simulation is conducted using a 512^3 grid, reaching a microscale Reynolds numbers of approximately 150, and $\alpha = -0.5$. Fig. 14 shows the temperature and density at one instant in time after the flow has reached stationary conditions and fully developed flow is obtained. In this configuration the problem is periodic in all directions allowing the use of pseudo-spectral discretization. This and other 3D simulations are documented in detail in [57]. We will not repeat the details here, simply to indicate that the approach introduced in earlier sections can be carried out without modifications to larger problems.

6. Conclusions

This paper presents an investigation of a numerical algorithm for the variable-density zero-Mach Navier-Stokes equations. The governing equations form a system of DAEs where the algebraic equation here is the state relationship for ideal gases under the zero-Mach number limit. The numerical algorithm is derived by following the standard procedure in DAE theory to first lower the differentiation index, which leads to a compatibility condition between the temperature and velocity fields. This compatibility condition is analogous to the divergence-free condition for incompressible problems; as it is well known. The derivation procedure of the mass constraint as well as subsequent pressure Poisson equation does not imply or use the chain rule of differentiation in spatial derivatives. Therefore, it is valid independent of the spatial discretization. This is different from the usual steps taken in the constant-density flows or previous work in the variable-density problems

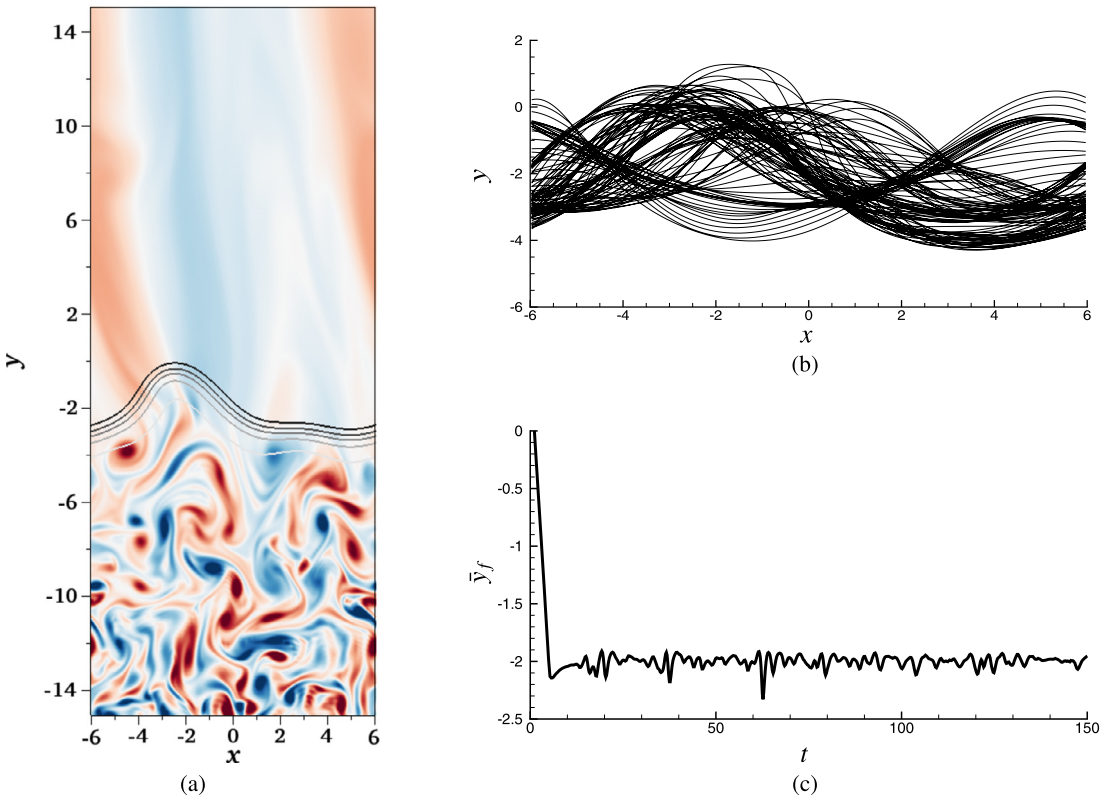

Fig. 13. (a) Flame profiles and vorticity fields (red and blue represent counter-clockwise and clockwise rotations respectively). (b) Instantaneous flame profiles ($T = 0.9$) with turbulent intensity of $u'/s_L = 0.5$ and $\mathcal{L} = 2$ (c) The time history of flame position.

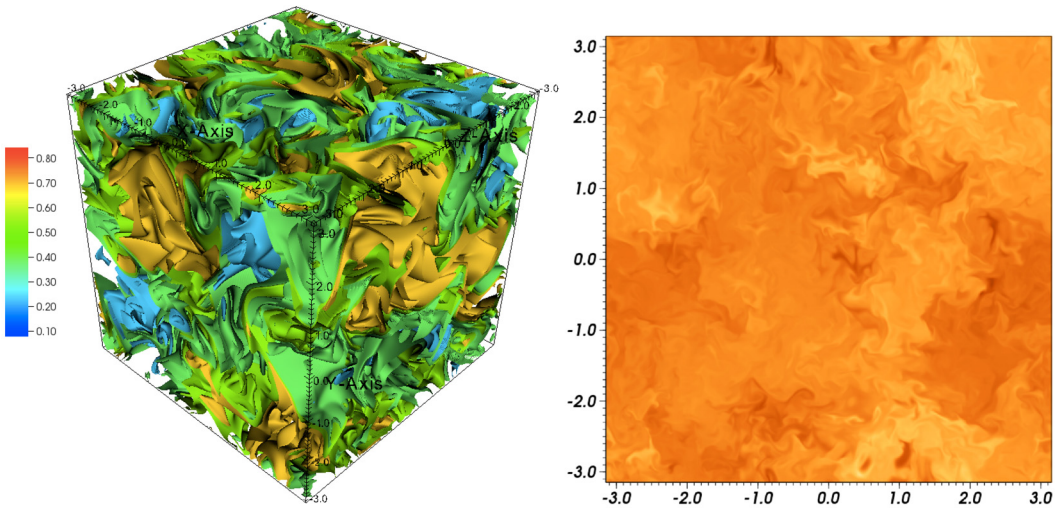

Fig. 14. Temperature (left) and density (right) from an instant in an isotropic turbulence simulation.

where the pressure Poisson equation is arrived by taking the divergence of momentum equation and invoking the algebraic constraint.

The numerical method for solving these derived equations are assessed extensively with the method of manufactured solutions in a periodic domain. Convergence rates of all field variables are uniform at the same order as the prescribed spatial discretization (2nd, 4th, and 6th orders, and pseudo-spectrally accurate) and time-integrator (2nd order Adams-Bashforth/Crank-Nicolson method). The main result being to point out that the null space of the adjoint of the Poisson equation is not simply the hydrostatic pressure mode, but a density-dependent vector.

Numerical stability is investigated with a forced variable-density flow problem. It is observed that the solver remains numerically stable for density ratios up to 20 and a reasonable CFL constraint. Other numerical properties such that mass conservation and comparative performance of iterative methods are also studied in details. Classical testing cases are also performed, which include the simulations of Rayleigh-Taylor flow, freely propagating premixed flames with incoming flow forcing, as well as a large-scale 3D variable-density turbulent mixing problem. The results show a good agreement with published data.

Declaration of competing interest

The authors declare that they have no known competing financial interests or personal relationships that could have appeared to influence the work reported in this paper.

Acknowledgements

This work was supported in part by the Air Force Office of Scientific Research under Grant No. FA9550-15-1-0035 (Dr. Chiping Li, Program Manager) and by the Department of Energy, National Nuclear Security Administration, under award No. DE-NA0002382, and the California Institute of Technology.

Appendix A. Boundary condition derivation

In this work, boundary condition treatment follows the methodologies reported in [49]. In this cited literature where constant-density incompressible flows are considered, the derived boundary condition leads to a solenoidal flow field. It is not the case with this zero-Mach number variable-density flow problem. Nonetheless, in propagating flame problems, density remains constant away from the flame surface, although inflow and outflow are at two different densities. Therefore, this section derives the boundary condition for such cases.

Consider an advection-diffusion equation for a generic scalar variable ϕ as follows,

$$\rho\left(\frac{\partial\phi}{\partial t}+\boldsymbol{u}\cdot\nabla\phi\right)=\frac{1}{Pe}\nabla^2\phi+\omega. \tag{A.1}$$

After integration-by-parts and rearranging terms, one obtains

$$\int_\Omega\frac{\rho}{2}\frac{\partial\|\phi\|^2}{\partial t}dV+\int_\Omega\frac{1}{Pe}\|\nabla\phi\|^2dV=\int_\Omega\left[\frac{\|\phi\|^2}{2}\nabla\cdot(\rho\boldsymbol{u})+\phi^T\omega\right]dV-\int_{\partial\Omega}\left[\frac{\|\phi\|^2}{2}\rho\boldsymbol{u}\cdot\boldsymbol{n}-\frac{1}{Pe}\phi^T\frac{\partial\phi}{\partial\boldsymbol{n}}\right]dS. \tag{A.2}$$

The integrand of boundary integral term can be expressed as

$$\|\phi\|^2\rho\boldsymbol{u}\cdot\boldsymbol{n}-\frac{2}{Pe}\phi^T\frac{\partial\phi}{\partial\boldsymbol{n}}=(\rho u_n)^{-1}\left((\rho u_n\phi)^2-\left(\frac{1}{Pe}\frac{\partial\phi}{\partial\boldsymbol{n}}\right)^2\right). \tag{A.3}$$

The boundary conditions for scalar variable ϕ is devised to ensure the positive sign of Eq. (A.3). One possible form proposed by [49] is given by

$$\lambda_0\phi-\frac{1}{Pe}\frac{\partial\phi}{\partial\boldsymbol{n}}=g_0, \tag{A.4}$$

and results in

$$-\int_{\partial\Omega}\left[\frac{\|\phi\|^2}{2}\rho\boldsymbol{u}\cdot\boldsymbol{n}-\frac{1}{Pe}\phi^T\frac{\partial\phi}{\partial\boldsymbol{n}}\right]dS=\int_{\partial\Omega}\frac{1}{|\rho u_n|}\left(g_0^2-(|\rho u_n|\,\phi+g_0)^2\right)dS, \tag{A.5}$$

where u_n denotes the normal velocity $\boldsymbol{u}\cdot\boldsymbol{n}$ and

$$\lambda_0=\frac{\rho u_n-|\rho u_n|}{2}. \tag{A.6}$$

Eq. (A.4) defines a boundary operator for the scalar variable. If the scalar variable at the boundaries ϕ_{bc} are explicitly given, g_0 is known and used. Otherwise, approximation to g_0 is required.

The boundary condition for the Navier-Stokes equations are derived in a similar approach. First, left-multiply the Navier-Stokes equations with $\boldsymbol{u}^T$ and integrate over the domain gives

$$\int_\Omega\rho\boldsymbol{u}^T\left(\frac{\partial\boldsymbol{u}}{\partial t}+\boldsymbol{u}\cdot\nabla\boldsymbol{u}\right)dV=\int_\Omega-\boldsymbol{u}^T\nabla p+\frac{1}{Re}\boldsymbol{u}^T\nabla^2\boldsymbol{u}+\rho\boldsymbol{u}^T\boldsymbol{f}\,dV. \tag{A.7}$$

Applying the integration by parts yields

$$\int_\Omega \rho \frac{\partial \|\boldsymbol{u}\|^2}{\partial t} dV + \int_\Omega \frac{2}{Re} \|\nabla \boldsymbol{u}\|^2 dV = \int_{\partial\Omega} \left(\frac{2}{Re} \boldsymbol{u}^T \frac{\partial \boldsymbol{u}}{\partial \boldsymbol{n}} - 2p\boldsymbol{u}\cdot\boldsymbol{n} - \|\boldsymbol{u}\|^2 \rho \boldsymbol{u}\cdot\boldsymbol{n} \right) dS + 2\int_\Omega \left(p\nabla\cdot\boldsymbol{u} + \frac{\|\boldsymbol{u}\|^2}{2}\nabla\cdot(\rho\boldsymbol{u}) + \rho\boldsymbol{u}^T\cdot\boldsymbol{f} \right) dV, \tag{A.8}$$

where the kinetic energy norm is the sum of its normal and tangential components $\|\boldsymbol{u}\|^2 = u_n^2 + u_t^2$.

The integrand of the boundary integral can be explicitly written out as

$$\frac{2}{Re}\left(u_n \frac{\partial u_n}{\partial \boldsymbol{n}} + u_t \frac{\partial u_t}{\partial \boldsymbol{n}} \right) - 2pu_n - \rho u_n (u_n^2 + u_t^2) = -W^T Z W, \tag{A.9}$$

where

$$W = \begin{bmatrix} u_n \\ u_t \\ p \\ \frac{1}{Re}\frac{\partial u_n}{\partial \boldsymbol{n}} \\ \frac{1}{Re}\frac{\partial u_t}{\partial \boldsymbol{n}} \end{bmatrix} \quad Z = \begin{bmatrix} \rho u_n & 0 & 1 & -1 & 0 \\ 0 & \rho u_n & 0 & 0 & -1 \\ 1 & 0 & 0 & 0 & 0 \\ -1 & 0 & 0 & 0 & 0 \\ 0 & -1 & 0 & 0 & 0 \end{bmatrix}. \tag{A.10}$$

The eigen-decomposition of the symmetric matrix Z gives the eigenvalues and eigenvectors of

$$\lambda_1 = \frac{\rho u_n}{2} + \sqrt{\left(\frac{\rho u_n}{2}\right)^2 + 1}, \quad q_1 = [0, -\lambda_1, 0, 0, 1]^T, \tag{A.11}$$

$$\lambda_2 = \frac{\rho u_n}{2} - \sqrt{\left(\frac{\rho u_n}{2}\right)^2 + 1}, \quad q_2 = [0, -\lambda_2, 0, 0, 1]^T, \tag{A.12}$$

$$\lambda_3 = 0, \quad q_3 = [0, 0, 1, 1, 0]^T, \tag{A.13}$$

$$\lambda_4 = \frac{\rho u_n}{2} + \sqrt{\left(\frac{\rho u_n}{2}\right)^2 + 2}, \quad q_4 = [-\lambda_4, 0, -1, 1, 0]^T, \tag{A.14}$$

$$\lambda_5 = \frac{\rho u_n}{2} - \sqrt{\left(\frac{\rho u_n}{2}\right)^2 + 2}, \quad q_5 = [-\lambda_5, 0, -1, 1, 0]^T. \tag{A.15}$$

The maximally dissipative form of the boundary conditions are constructed to suppress the negative eigenvalues (i.e. λ_2 and λ_5), which yields

$$\lambda_2 u_t - \frac{1}{Re}\frac{\partial u_t}{\partial \boldsymbol{n}} = g_2, \tag{A.16}$$

$$\lambda_5 u_n - \frac{1}{Re}\frac{\partial u_n}{\partial \boldsymbol{n}} + p = g_5. \tag{A.17}$$

Note that Eq. (A.4), Eq. (A.16), and Eq. (A.17) are viable boundary formulations that lead to energy-stability. These boundary operators derived are simple extension to those in [49], expect we carry the constant density near the boundaries while computing eigenvalues λ's. Other forms are also possible, for instance, zero-gradient at the outflow boundary, see [58]. These formulations has implicitly defined the continuous boundary operators $\mathcal{B}$ for scalar variables, normal and tangential velocities, and pressure. These conditions are imposed using a penalty-based method by adding SAT terms to the discretized governing equations, discussed in the next section.

Appendix B. SAT terms

Consider a one-dimensional model problem in $\Omega = [-L/2, L/2]$

$$\frac{\partial u}{\partial t} + \nabla u - \nu \nabla^2 u = 0, \tag{B.1}$$

$$u(x, 0) = u_0, \quad x \in \Omega, \tag{B.2}$$

$$\mathcal{B}u = g, \quad x \in \partial\Omega. \tag{B.3}$$

The spatial discretization matrices are defined as: (1) $D = H^{-1}Q$ approximates $\frac{d}{dx}$, (2) $D^2 = H^{-1}(-M + BS)$ approximates $\frac{d^2}{dx^2}$. H is a norm operator, $B = \text{diag}[-1, 0, \ldots, 0, 1]$, and S is a biased stencil at the boundary that provides approximation

to $\frac{d}{dx}$. Furthermore, $Q + Q^T = B$ and $M = M^T \geq 0$ are spatial discretization of first and second order derivatives for interior points. The detailed matrices for different orders of accuracy of Q, H, M, B, and S can be found in [46]. In this work, we use the diagonal norm operators, that being said, H is a diagonal matrix and SAT terms only enter the first and last rows in non-periodic direction.

Applying the SAT methods to this initial-boundary-value problem, the semi-discretized equation are given by

$$\frac{\partial u}{\partial t} = -H^{-1}Qu + \nu H^{-1}(-M + BS)u + \tau_1 H^{-1} e_1 \otimes Lu + \tau_N H^{-1} e_N \otimes Lu, \tag{B.4}$$

where L represents the discrete counterpart of the continuous boundary operator $\mathcal{B}$ and τ_1 and τ_2 are penalty parameters. e_1 and e_N denotes vector $[1, 0, \ldots, 0]$ and $[0, \ldots, 0, 1]$, respectively. The last two terms in Eq. (B.4) are penalty terms, often known as SAT terms.

One can understand the summation-by-parts property of the spatial matrices by applying discrete energy method to the governing equation as

$$\frac{\partial \|u\|_H^2}{\partial t} + \nu u^T M u = -\frac{1}{2} u^T (Q + Q^T) u + \nu u^T (BS + (BS)^T) u + \tau_1 u^T e_1 \otimes Lu + \tau_N u^T e_N \otimes Lu, \tag{B.5}$$

$$= u^T e_1 \otimes (\frac{1}{2} u - \nu BSu + \tau_1 Lu) - u^T e_N \otimes (\frac{1}{2} u - \nu BSu + \tau_N Lu). \tag{B.6}$$

$\frac{1}{2}u - \nu BSu$ appears in the right hand side is the counterpart of the boundary integral terms in the continuous problem after applying the integral-by-parts operations. SAT terms is responsible to cancel the wrong sign at the right hand side. Let $Lu_1 = \frac{1}{2}u_1 - \nu BSu_1$ and $Lu_N = -\nu BSu_N$, the energy estimate is bounded if $\tau_1 \leq -1$ and $\tau_N \geq 1$.

Appendix A derived Eq. (A.4), Eq. (A.16), and Eq. (A.17) as the suitable boundary conditions for variable-density zero-Mach number Navier-Stokes equations that lead to stable energy estimate. These conditions are imposed by formulating the corresponding SAT terms and incorporated into the numerical methods presented in this work. The SAT terms used in Eq. (15) and Eq. (16) are given by

$$S_\rho = \frac{\tau_1}{\rho} e_1 \otimes L + \frac{\tau_N}{\rho} e_N \otimes L, \tag{B.7}$$

where

$$L\phi = \lambda_0(\phi - \phi_{bc}) - \frac{1}{Pe} BS\phi, \quad Lu_t = \lambda_2(u_t - u_{t,bc}) - \frac{1}{Re} BSu_t, \quad Lu_n = \lambda_5(u_n - u_{n,bc}) - \frac{1}{Re} BSu_n + p - p_{bc}, \tag{B.8}$$

and

$$\lambda_0 = \frac{\rho u_n - |\rho u_n|}{2}, \quad \lambda_2 = \frac{\rho u_n}{2} - \sqrt{\left(\frac{\rho u_n}{2}\right)^2 + 1}, \quad \lambda_5 = \frac{\rho u_n}{2} - \sqrt{\left(\frac{\rho u_n}{2}\right)^2 + 2}. \tag{B.9}$$

Note that in principle the gradient of primitive variables at the boundaries are assumed to be zero. ϕ_{bc}, $u_{n,bc}$, $u_{t,bc}$, and p_{bc} are boundary data vectors, whose sizes are same as field variables, but only non-zero at boundary points. Here we have also included the pressure terms for generality. However, in practice, one may employ Neumann-type boundary conditions for pressure. In that case, pressure term does not appear in the SAT terms.

Since the time integrator used in this work is semi-implicit, therefore, the SAT terms resulted from diffusion and pressure gradient terms are also treated implicitly while advection SAT terms are explicit. SAT terms defined in Eq. (17) are given by

$$S_\rho^a \phi = \frac{\tau_1}{\rho} e_1 \otimes \lambda_0(\phi - \phi_{bc,1}) + \frac{\tau_N}{\rho} e_N \otimes \lambda_0(\phi - \phi_{bc,N}), \qquad S_\rho^d \phi = -\frac{1}{Pe}\frac{\tau_1}{\rho} e_1 \otimes BS\phi - \frac{1}{Pe}\frac{\tau_N}{\rho} e_N \otimes BS\phi, \tag{B.10}$$

$$S_\rho^a u_t = \frac{\tau_1}{\rho} e_1 \otimes \lambda_2(u_t - u_{t,bc,1}) + \frac{\tau_N}{\rho} e_N \otimes \lambda_2(\phi - \phi_{bc,N}), \qquad S_\rho^d u_t = -\frac{1}{Re}\frac{\tau_1}{\rho} e_1 \otimes BSu_t - \frac{1}{Re}\frac{\tau_N}{\rho} e_N \otimes BSu_t, \tag{B.11}$$

$$S_\rho^a u_n = \frac{\tau_1}{\rho} e_1 \otimes \lambda_5(u_n - u_{n,bc,1}) + \frac{\tau_N}{\rho} e_N \otimes \lambda_5(u_n - u_{n,bc,N}) \quad S_\rho^d u_n = -\frac{1}{Re}\frac{\tau_1}{\rho} e_1 \otimes BSu_n - \frac{1}{Re}\frac{\tau_N}{\rho} e_N \otimes BSu_n, \tag{B.12}$$

and

$$S_\rho^g u_n = \frac{\tau_1}{\rho} e_1 \otimes (\tilde{p} - p_{bc,1}) + \frac{\tau_N}{\rho} e_N \otimes (\tilde{p} - p_{bc,N}), \tag{B.13}$$

where $\tilde{p}$ denotes the numerical boundary value of pressure. The procedure to compute $\tilde{p}$ can be found in [49]. In practice, the pressure data for an inflow/outflow problem is usually unknown. As mentioned above, when homogeneous Neumann boundary conditions are imposed to the pressure Poisson equations and SAT terms associated with pressure do not enter the momentum equations. That is to say, one or both of terms in Eq. (B.13) is zero.

Appendix C. Iterative solution of the system

An iterative approach for the linear system is more practical in large-scale simulations because of the smaller memory requirements and overall faster calculation. We formulate an iterative scheme under a quasi-Newton strategy with different choices for the approximate Jacobian to facilitate comparisons. The quasi-Newton iteration can be stated as

$$\boldsymbol{x}_{l+1} = \boldsymbol{x}_l + \delta\boldsymbol{x}, \quad \mathscr{J}\,\delta\boldsymbol{x} = \boldsymbol{b}_w - \mathcal{A}\boldsymbol{x}_l, \tag{C.1}$$

where l denotes the iteration number and $\mathscr{J}$ is the approximate Jacobian matrix. The following common approximations to the Jacobian are considered here

$$\mathscr{J}_0 = \begin{bmatrix} \boldsymbol{A}_{\rho^{n+1}} & 0 \\ 0 & -\frac{1}{\rho^{n+1}}\nabla_h^2 \end{bmatrix}, \quad \mathscr{J}_1 = \begin{bmatrix} \boldsymbol{A}_{\rho^{n+1}} & 0 \\ 0 & -(Q_{\rho^{n+1}} R\boldsymbol{G}_{\rho^{n+1/2}})^* \end{bmatrix}, \quad \mathscr{J}_2 = \begin{bmatrix} \boldsymbol{A}_{\rho^{n+1}} & G_{\rho^{n+1/2}} \\ 0 & -(Q_{\rho^{n+1}} R\boldsymbol{G}_{\rho^{n+1/2}})^* \end{bmatrix}. \tag{C.2}$$

Although there are an infinite number of similarity transformations that one can exploit to approximate the Jacobian, these approximations benefit from their simple structural properties. For example, $\mathscr{J}_0$ is symmetric and easy-to-assemble while $\mathscr{J}_1$ and $\mathscr{J}_2$ lead to iterative matrices $I - \mathscr{J}^{-1}\mathcal{A}$ whose spectral radius are comparatively small. A fourth iteration constructed by retaining the lower left corner block of $\mathcal{A}$ and zeroing the upper right corner block is equivalent to $\mathscr{J}_2$ but more computationally expensive because $G_{\rho^{n+1/2}}$ is easier to construct. Furthermore, we also observe that replacing the skew-symmetric advection operator in $Q_{\rho^{n+1}}$ by the advective form does not degrade the performance of the iteration. The different choices result in different performances which are detailed below in a concrete example.

Numerical experiments are also used to compare the performance of the different approximated Jacobians, Eq. (C.2), introduced as part of quasi-Newton formulations to solve Eq. (37) using block iterations discussed in Appendix C. All iteration choices converge to machine precision, if allowed, even for density variations of $r = \rho_{max}/\rho_{min} = 20$. We now set the relative tolerance of the residual to 10^{-12}, which is characteristic of a typical well-converged simulation, and assess the number of quasi-Newton iterations N that are required for different choices of Jacobian and density ratios.

The numerical tests use the mesh with 64×64 grid points and 4th order finite-difference spatial discretization (similar results are obtained for the other discretizations). The manufactured solution problem in § 4.1 is used with parameters of $Re = 100$, $Pe = 100$, and $\omega = 2\pi$. The numerical integration advances with a fixed time-step size up to $t = 1$ with an initial CFL of 0.5. Fig. C.15 shows the number of quasi-Newton iterations, N (vertical axis), vs flow time, t (horizontal axis), required to achieve the target relative residual for density ratios 4, 10, and 20. One observes that the $\mathscr{J}_2$ Jacobian outperforms all others (for all density ratios). Next, it is observed that the iterations that use $(Q_{\rho^{n+1}} R\boldsymbol{G}_{\rho^{n+1/2}})^*$ converge faster than those using the constant-coefficient Laplacian-like operator. Furthermore, we verify that the convergence speed is improved by the presence of the advective component of $Q_{\rho^{n+1}}$, which is very similar (although not discretely equivalent) to using a variable-coefficient Laplacian-like operator of the form $\nabla_h \cdot [\rho^{n+1}]^{-1}\nabla_h$, see Eq. (36). Finally, the difference between $\mathscr{J}_1$ and $\mathscr{J}_2$ is caused by the extra off-diagonal block in the latter, since a partial iteration for the pressure is used immediately to update the velocity. Importantly, note that the simple iteration using the block diagonalized Jacobian, $\mathscr{J}_0$, degrades with increasing density ratio. This highlights that too much simplification in the Jacobian leads to a loss of information of the coupling introduced by density and this costs in terms of more iterations required to achieve convergence.

The numerical experiments also indicate that the proposed method is capable of solving problems with relatively high density ratios. Fig. C.16 shows the iteration numbers required to reach convergence as a function of density ratios. Here approximated Jacobian $\mathscr{J}_2$ is used and the mesh size is increased to 128×128 grid points such that solutions are well-represented even when the density ratio increases up to 500. Plot (c) in Fig. C.16 shows the maximum number iteration required for increasing density ratios. A linear fitting of these observed data suggests $N \sim \exp^{0.5\log(r)+0.7}$.

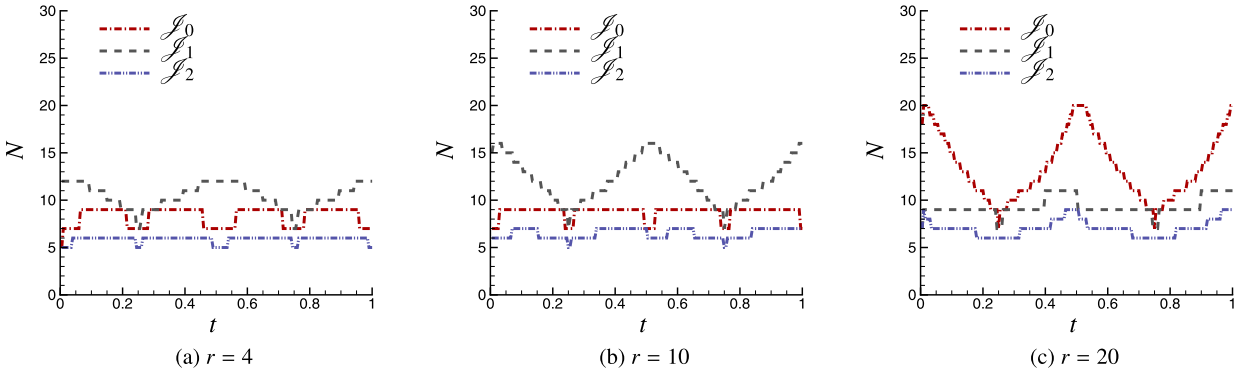

Fig. C.15. Comparison of approximate Jacobians in the convergence of the quasi-Newton iteration for different density ratios as a function of time.

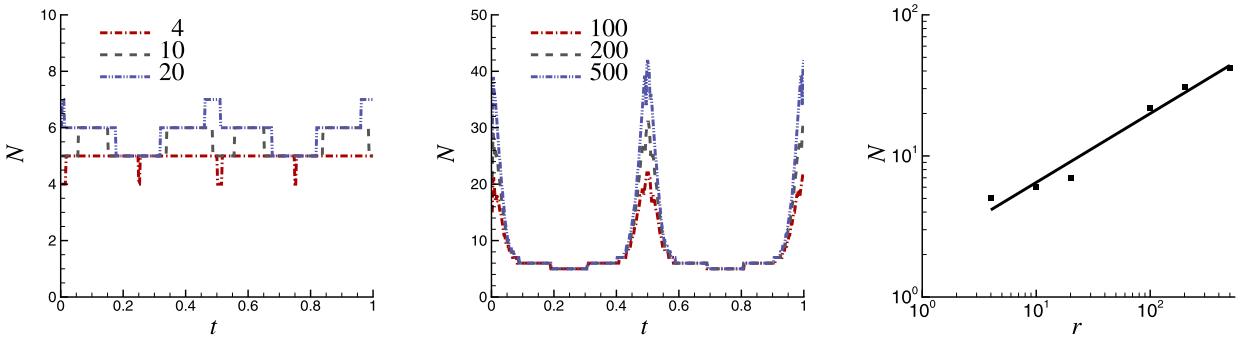

(a) Low density ratios (b) High density ratios (c) Max iteration numbers

Fig. C.16. Comparison of iteration numbers as a function of increasing density ratios.

References

[1] P. Gresho, R. Sani, Incompressible Flow and the Finite Element Method, vol. 2, John Wiley and Sons, Inc., New York, NY (United States), 1998.
[2] M.O. Deville, P.F. Fischer, E.H. Mund, High-Order Methods for Incompressible Fluid Flow, vol. 9, Cambridge University Press, 2002.
[3] R. Temam, Navier-Stokes Equations: Theory and Numerical Analysis, vol. 343, American Mathematical Soc., 2001.
[4] J.-L. Guermond, P. Minev, J. Shen, An overview of projection methods for incompressible flows, Comput. Methods Appl. Mech. Eng. 195 (2006) 6011–6045.
[5] Y. Hou, K. Mahesh, A robust, colocated, implicit algorithm for direct numerical simulation of compressible, turbulent flows, J. Comput. Phys. 205 (2005) 205–221.
[6] A. Majda, J. Sethian, The derivation and numerical solution of the equations for zero Mach number combustion, Combust. Sci. Technol. 42 (1985) 185–205.
[7] G.E. Karniadakis, M. Israeli, S.A. Orszag, High-order splitting methods for the incompressible Navier-Stokes equations, J. Comput. Phys. 97 (1991) 414–443.
[8] A.S. Almgren, J.B. Bell, P. Colella, L.H. Howell, M.L. Welcome, A conservative adaptive projection method for the variable density incompressible Navier–Stokes equations, J. Comput. Phys. 142 (1998) 1–46.
[9] J.-L. Guermond, A. Salgado, A fractional step method based on a pressure Poisson equation for incompressible flows with variable density, C. R. Math. 346 (2008) 913–918.
[10] J.-H. Pyo, J. Shen, Gauge–Uzawa methods for incompressible flows with variable density, J. Comput. Phys. 221 (2007) 181–197.
[11] J.-L. Guermond, A. Salgado, A splitting method for incompressible flows with variable density based on a pressure Poisson equation, J. Comput. Phys. 228 (2009) 2834–2846.
[12] S. Pirozzoli, Generalized conservative approximations of split convective derivative operators, J. Comput. Phys. 229 (2010) 7180–7190.
[13] D. Modesti, S. Pirozzoli, An efficient semi-implicit solver for direct numerical simulation of compressible flows at all speeds, J. Sci. Comput. 75 (2018) 308–331.
[14] G. Coppola, F. Capuano, S. Pirozzoli, L. de Luca, Numerically stable formulations of convective terms for turbulent compressible flows, J. Comput. Phys. 382 (2019) 86–104.
[15] F. Nicoud, Conservative high-order finite-difference schemes for low-Mach number flows, J. Comput. Phys. 158 (2000) 71–97.
[16] D. Livescu, J.R. Ristrorcelli, Buoyancy-driven variable-density turbulence, J. Fluid Mech. 591 (2007).
[17] E. Motheau, J. Abraham, A high-order numerical algorithm for DNS of low-Mach-number reactive flows with detailed chemistry and quasi-spectral accuracy, J. Comput. Phys. 313 (2016) 430–454.
[18] J. Doom, Y. Hou, K. Mahesh, A numerical method for DNS/LES of turbulent reacting flows, J. Comput. Phys. 226 (2007) 1136–1151.
[19] J.B. Bell, D.L. Marcus, A second-order projection method for variable-density flows, J. Comput. Phys. 101 (1992) 334–348.
[20] B. Lessani, M.V. Papalexandris, Time-accurate calculation of variable density flows with strong temperature gradients and combustion, J. Comput. Phys. 212 (2006) 218–246.
[21] O. Desjardins, G. Blanquart, G. Balarac, H. Pitsch, High order conservative finite difference scheme for variable density low Mach number turbulent flows, J. Comput. Phys. 227 (2008) 7125–7159.
[22] C.D. Pierce, P. Moin, Progress-variable approach for large-eddy simulation of non-premixed turbulent combustion, J. Fluid Mech. 504 (2004) 73–97.
[23] D. Chung, D.I. Pullin, Direct numerical simulation and large-eddy simulation of stationary buoyancy-driven turbulence, J. Fluid Mech. 643 (2010).
[24] A.W. Cook, J.J. Riley, Direct numerical simulation of a turbulent reactive plume on a parallel computer, J. Comput. Phys. 129 (1996) 263–283.
[25] M. Hassanaly, H. Koo, C.F. Lietz, S.T. Chong, V. Raman, A minimally-dissipative low-Mach number solver for complex reacting flows in openfoam, Comput. Fluids 162 (2018) 11–25.
[26] M. Benzi, G.H. Golub, J. Liesen, Numerical solution of saddle point problems, Acta Numer. 14 (2005) 1–137.
[27] P.M. Gresho, R.L. Sani, On pressure boundary conditions for the incompressible Navier-Stokes equations, Int. J. Numer. Methods Fluids 7 (1987) 1111–1145.
[28] J. de Charentenay, D. Thévenin, B. Zamuner, Comparison of direct numerical simulations of turbulent flames using compressible or low-Mach number formulations, Int. J. Numer. Methods Fluids 39 (2002) 497–515.
[29] H.N. Najm, O.M. Knio, Modeling low Mach number reacting flow with detailed chemistry and transport, J. Sci. Comput. 25 (2005) 263.
[30] O.M. Knio, H.N. Najm, P.S. Wyckoff, A semi-implicit numerical scheme for reacting flow: II. Stiff, operator-split formulation, J. Comput. Phys. 154 (1999) 428–467.
[31] H.N. Najm, P.S. Wyckoff, O.M. Knio, A semi-implicit numerical scheme for reacting flow: I. Stiff chemistry, J. Comput. Phys. 143 (1998) 381–402.
[32] R. Yu, J. Yu, X.-S. Bai, An improved high-order scheme for DNS of low Mach number turbulent reacting flows based on stiff chemistry solver, J. Comput. Phys. 231 (2012) 5504–5521.
[33] J. Fröhlich, R. Peyret, Direct spectral methods for the low Mach number equations, Int. J. Numer. Methods Heat Fluid Flow 2 (1992) 195–213.
[34] C. Rhie, W. Chow, A numerical study of the turbulent flow past an isolated airfoil with trailing edge separation, in: AIAA-82-0998, AIAA/ASME 3rd Joint Thermophysics, Fluids, Plasma and Heat Transfer Conference, St Louis, Missouri, 1982.
[35] E. Dick, A flux-vector splitting method for steady Navier-Stokes equations, Int. J. Numer. Methods Fluids 8 (1988) 317–326.

[36] P. Rauwoens, J. Vierendeels, B. Merci, A solution for the odd–even decoupling problem in pressure-correction algorithms for variable density flows, J. Comput. Phys. 227 (2007) 79–99.
[37] A. Prosperetti, G. Tryggvason, Computational Methods for Multiphase Flow, Cambridge University Press, 2009.
[38] K.E. Brenan, S.L. Campbell, L.R. Petzold, Numerical Solution of Initial-Value Problems in Differential-Algebraic Equations, vol. 14, SIAM, 1996.
[39] P.J. Rabier, W.C. Rheinboldt, Theoretical and Numerical Analysis of Differential-Algebraic Equations, Elsevier, 2002.
[40] R. Temam, Suitable initial conditions, J. Comput. Phys. 218 (2006) 443–450.
[41] F.H. Harlow, J.E. Welch, Numerical calculation of time-dependent viscous incompressible flow of fluid with free surface, Phys. Fluids 8 (1965) 2182–2189.
[42] D. Livescu, J. Ristorcelli, Variable-density mixing in buoyancy-driven turbulence, J. Fluid Mech. 605 (2008) 145–180.
[43] D.C.D.R. Fernández, J.E. Hicken, D.W. Zingg, Review of summation-by-parts operators with simultaneous approximation terms for the numerical solution of partial differential equations, Comput. Fluids 95 (2014) 171–196.
[44] M. Svärd, J. Nordström, Review of summation-by-parts schemes for initial–boundary-value problems, J. Comput. Phys. 268 (2014) 17–38.
[45] B. Strand, Summation by parts for finite difference approximations for d/dx, J. Comput. Phys. 110 (1994) 47–67.
[46] K. Mattsson, J. Nordström, Summation by parts operators for finite difference approximations of second derivatives, J. Comput. Phys. 199 (2004) 503–540.
[47] R. Temam, Une méthode d'approximation de la solution des équations de Navier-Stokes, Bull. Soc. Math. Fr. 98 (1968) 115–152.
[48] Y. Morinishi, Skew-symmetric form of convective terms and fully conservative finite difference schemes for variable density low-Mach number flows, J. Comput. Phys. 229 (2010) 276–300.
[49] J. Nordström, K. Mattsson, C. Swanson, Boundary conditions for a divergence free velocity–pressure formulation of the Navier-Stokes equations, J. Comput. Phys. 225 (2007) 874–890.
[50] G. Strang, On the construction and comparison of difference schemes, SIAM J. Numer. Anal. 5 (1968) 506–517.
[51] S. Badia, R. Codina, Algebraic pressure segregation methods for the incompressible Navier-Stokes equations, Arch. Comput. Methods Eng. 15 (2007) 1–52.
[52] J.-L. Guermond, L. Quartapelle, A projection FEM for variable density incompressible flows, J. Comput. Phys. 165 (2000) 167–188.
[53] C. Calgaro, E. Creuse, T. Goudon, An hybrid finite volume-finite element method for variable density incompressible flows, J. Comput. Phys. 227 (2008) 4671–4696.
[54] A.W. Cook, W. Cabot, P.L. Miller, The mixing transition in Rayleigh-Taylor instability, J. Fluid Mech. 511 (2004) 333–362.
[55] J.-L. Guermond, R. Pasquetti, Entropy-based nonlinear viscosity for Fourier approximations of conservation laws, C. R. Math. 346 (2008) 801–806.
[56] N. Fogla, F. Creta, M. Matalon, Influence of the Darrieus-Landau instability on the propagation of planar turbulent flames, Proc. Combust. Inst. 34 (2013) 1509–1517.
[57] D. Petty, C. Pantano, A semi-lagrangian direct-interaction closure of the spectra of isotropic variable-density turbulence, J. Fluid Mech. 876 (2019) 186–236.
[58] H.-O. Kreiss, J. Lorenz, Initial-Boundary Value Problems and the Navier-Stokes Equations, vol. 47, SIAM, 1989.